DRD No. SE7
DRL No. 58

SILICON MATERIALS TASK OF THE LOW-COST SOLAR ARRAY PROJECT (PHASE IV)

Effects of Impurities and Processing on Silicon Solar Cells

Twenty-Second Quarterly Report

April, 29, 1981

JPL NO. 9950-558

January 1981-March 1981

Dist. Cat. UC-63
DOE/JPL 954331-81-14

R. H. Hopkins, M. H. Hanes, J. R. Davis, A. Rohatgi, and P. Rai-Choudhury
Westinghouse Research and Development Center
and
H. C. Mollenkopf
Hemlock Semiconductor Corporation

Contract No. 954331

The JPL Low-Cost Silicon Solar Array Project is sponsored by the U. S. Department of Energy and forms part of the Solar Photovoltaic Conversion Program to initiate a major effort toward the development of low-cost solar arrays. This work was performed for the Jet Propulsion Laboratory, California Institute of Technology by agreement between NASA and DOE.

Westinghouse R&D Center
1310 Beulah Road
Pittsburgh, Pennsylvania 15235

DRD No. SE7
DRL No. 58

SILICON MATERIALS TASK OF THE LOW-COST SOLAR ARRAY PROJECT (PHASE IV)

Effects of Impurities and Processing on Silicon Solar Cells

Twenty-Second Quarterly Report

April, 29, 1981

January 1981-March 1981

Dist. Cat. UC-63
DOE/JPL 954331-81 14

R. H. Hopkins, M. H. Hanes, J. R. Davis, A. Rohatgi, and P. Rai-Choudhury
Westinghouse Research and Development Center
and
H. C. Mollenkopf
Hemlock Semiconductor Corporation

Contract No. 954331

The JPL Low-Cost Silicon Solar Array Project is sponsored by the U. S. Department of Energy and forms part of the Solar Photovoltaic Conversion Program to initiate a major effort toward the development of low-cost solar arrays. This work was performed for the Jet Propulsion Laboratory, California Institute of Technology by agreement between NASA and DOE.

Westinghouse R&D Center
1310 Beulah Road
Pittsburgh, Pennsylvania 15235

TECHNICAL CONTENT STATEMENT

This report was prepared as an account of work sponsored by the United States Government. Neither the United States nor the United States Department of Energy, nor any of their employees, nor any of their contractors, sub-contractors, or their employees, makes any warranties, express or implied, or assumes any legal liability or responsibility for the accuracy, completeness or usefulness of any information, apparatus, product or process disclosed, or represents that its use would not infringe privately owned rights.

NEW TECHNOLOGY

No new technology is reportable for the period covered by this report.

TABLE OF CONTENTS

		Page
1.	SUMMARY	1
2.	INTRODUCTION	3
3.	TECHNICAL PROGRESS	5
	3.1 Crystal Growth and Analysis	5
	3.1.1 Ingot Preparation	5
	3.1.2 Ingot Evaluation	13
	3.1.3 Impurity-induced Structural Breakdown	13
	3.2 The Permanence of Impurity Effects in Silicon Solar Cells	18
	3.2.1 Mechanism of High-Temperature Aging	18
	3.2.2 Electrical Bias Effects	23
	3.3 Thermochemical Processing	25
	3.3.1 Ion Implant-Induced Damage Gettering	25
	3.3.1.1 Experimental Sequence	25
	3.3.1.2 Gettering of Copper	34
	3.3.1.3 Gettering of Titanium	37
	3.3.1.4 Conclusions	37
	3.3.2 Impurity Response to N_2 Heat Treatment	40
	3.4 Solar Cell and Material Evaluation by DLTS	45
	3.5 Impurity Effects in High-Efficiency Solar Cells	46
4.	CONCLUSIONS	57
5.	PROGRAM STATUS	59
	5.1 Present Status	59
	5.2 Future Activity	59
6.	REFERENCES	61
7.	ACKNOWLEDGEMENTS	62

LIST OF FIGURES

Figure		Page
1	Transformed I-V Curves for Ag-Doped Solar Cells Before and After Aging 10 Hours at 400°C.	21
2	Effect of Electrical Bias on Relative Efficiency as a Function of Stress Temperature-Base Line Cells	26
3	Effect of Electrical Bias on Relative Efficiency as a Function of Stress Temperature-Fe-Doped (1.06×10^{15} cm^{-3}) Cells.	27
4	Effect of Electrical Bias on Relative Efficiency as a Function of Stress Temperature-Nb-Doped ($<0.44 \times 10^{15}$ cm^{-3}) Cells.	28
5	Effect of Electrical Bias on Relative Efficiency as a Function of Stress Temperature-Ag-Doped (2.20×10^{15} cm^{-3}) Cells.	29
6	Effect of Electrical Bias on Relative Efficiency as a Function of Stress Temperature-Cr-Doped (1.04×10^{15} cm^{-3}) Cells.	30
7	Effect of Electrical Bias on Relative Efficiency as a Function of Stress Temperature-Fe-Doped (0.4×10^{15} cm^{-3}) Cells.	31
8	Effect of Electrical Bias on Relative Efficiency as a Function of Stress Temperature-Cu-Doped (65×10^{15} cm^{-3}) Cells.	32
9	Effect of Electrical Bias on Relative Efficiency as a Function of Stress Temperature-Nb-Doped ($<0.009 \times 10^{15}$ cm^{-3}) Cells.	33
10	Effects of HCℓ and Ion Implant Damage Gettering on Solar Cell Material Containing Copper.	35
11	Effects of $POCℓ_3$ and Ion Implant Damage Gettering on Solar Cell Material Containing Copper.	36
12	Effects of HCℓ and Ion Implant Damage Gettering on Solar Cell Material Containing Titanium.	38

LIST OF FIGURES (Cont.)

Figure		Page
13	Effects of $POC\ell_3$ and Ion Implant Damage Gettering on Solar Cell Material Containing Titanium.	39
14	Change in Electrically Active Impurity Concentration After an 825°C/1 hr N_2 Anneal.	41
15	Variation of Electrically Active Cr Concentration Following a One-Hour Treatment in N_2	42
16	Calculated Cell Efficiency as a Function of Molybdenum Concentration for a Standard (SE) Design Cell (η = 14%, W_B = 275μm.)	49
17	Calculated Efficiency as a Function of Molybdenum Concentration for a Narrow Base, Back Surface Field HE Cell (η = 15.35%, W_B = 150μm).	50
18	Phase IV Program Plan Schedule	60

LIST OF TABLES

Table		Page
1	Ingot Impurity, Structure and Task.	5
2	Ingot Impurity Concentration.	6
3	Best Estimate of Impurity Concentrations.	8
4	Ingot Electrical and Defect Characteristics	10
5	Ingot Carbon and Oxygen Concentrations.	12
6	Comparison of Critical Impurity Concentrations for Structural Breakdown in Single and Polycrystalline Ingots .	15
7	Diffusion Constants for Metals in Liquid Silicon Calculated From Ingot Breakdown Data	16
8	Cell Data for Ag And Cr-Doped Solar Cells Employed in Aging Tests	19
9	DLTS Results After Aging Treatments (N_2 Atmosphere) Performed on Ag and Cr-Doped Samples.	20
10	Silicon Ingots Undergoing Electrical Bias Solar Cell Testing	24
11	The Effect of N_2 Heat Treatment on the Electrically Active Cr Concentration at the Surface of Wafers Containing 1×10^{15} cm^{-3} Metallurgical Cr.	43
12	DLTS Results on Impurity-Doped Ingots	44
13	Properties of Standard Process Cells.	47
14	High-Efficiency Cell Types Under Investigation.	48
15	100μm Cells with BSF and Ohmic Backs, Averaged Data	51
16	100μm Cells with BSF and Gridded Back (See Text), Averaged Data.	52

1. SUMMARY

The overall objective of this program is to define the effects of impurities, various thermochemical processes, and any impurity-process interactions upon the performance of terrestrial solar cells. The results of the study form a basis for silicon producers, wafer manufacturers, and cell fabricators to develop appropriate cost-benefit relationships for the use of less pure, less costly solar grade silicon.

We have confirmed—at least for V, Mo, and Cr— that impurity-induced ingot structure breakdown occurs at a lower liquid-impurity concentration for polycrystalline ingots than when growing single crystal ingots. The threshold impurity concentration for breakdown, C_ℓ^*, is 2 to 10 times smaller for poly ingot growth.

Using a model which relates the measured value of C_ℓ^* to crystal growth rate, crystal diameter, and impressed thermal gradient, we have calculated the value of the liquid diffusion constant, D, for several metal impurities studied. D ranges between 1.5 and 4.2 x 10^{-4} cm^2/sec for the impurities Gd, Zr, Mo, W, V, Ti, Fe, Co, Pd, Ag and Cu. These values are close to those reported in the literature for metal diffusion in liquid silicon.

DLTS measurements were employed to identify the mechanism of solar cell performance reduction observed during accelerated (high-temperature) aging tests. For Ag and Cr-doped solar cells, respectively, cell efficiency loss correlates with a reduction in bulk minority-carrier lifetime and the formation of deep levels which did not appear in the devices prior to aging at elevated temperature.

We continue to observe no significant performance reduction in solar cells aged at low temperature under electrical bias. Samples doped with Fe, Nb, Cr, Ti, Ag and Cu were aged 100 hours at eleven different temperatures up to 245°C with no effect.

Ar implant damage combined with HCℓ or $POCℓ_3$ gettering raises the efficiency of Ti-doped cells by 0.5 to 1% (absolute) compared to the ungettered devices. However, the HCℓ or $POCℓ_3$ treatments by themselves are somewhat more effective. Ar implant plus heat treatment at 1100°C also improves device performance but not as much as the combined treatments. For Cu-doped devices, increasing gettering temperature increases cell performance. However, neither the combined treatment nor HCℓ (or $POCℓ_3$) alone raises cell performance to that of the ungettered devices.

Heat treatment of Cr-doped silicon in N_2 at temperatures between 100 and 600°C for one hour produces a montonic drop in the electrically active Cr concentration as the treatment temperature is raised. Above about 500°C no electrically active Cr is observed by DLTS.

Data from 100 μm-thick vanadium-doped BSF solar cells are in good agreement with our impurity model predictions which forecast that the increased sensitivity due to impurity effect can be ameliorated somewhat on thin cells.

2. INTRODUCTION

This is the twenty-second quarterly report describing activities conducted under JPL Contract 954331, and is the fifth report of the Phase IV studies.

In Phase III, "An Investigation of the Effects of Impurities and Processing on Silicon Solar Cells," the effects of thermal processes, impurities, and impurity-process interactions were determined and documented. The development of this data base led to a more precise definition of what constitutes an acceptable "Solar Grade" Silicon. In addition, it provided silicon manufacturers with a rationale for selection of construction materials; it has helped ingot, sheet, or ribbon manufacturers to specify the purity of silicon feedstocks; it has enabled cell manufacturers to define acceptable wafer purities for cell fabrication and to choose processes which minimize adverse impurity effects. In short, the impurity-effect data provide a basis for cost-benefit analysis to producers and users of Solar Grade Silicon.

In Phase IV of this program, the approaches and techniques developed in Phase III are being extended to several new areas, as well as to developing an improved data base for aging effects and certain process-related phenomena. The Phase IV tasks include (1) evaluation, by previously developed process techniques, of the properties of silicon produced by experimental low-cost processes; (2) extending threshold impurity concentration data to high-efficiency cells; (3) measuring the effects of interaction between impurities and grain boundaries in polycrystalline solar cells; (4) evaluating the long-term effects of impurities in solar cells; and (5) examining the effects of processes such as ion implantation on contaminated solar cells.

During this quarter we have continued the studies of polycrystalline solar cells, accelerated aging of impurity behavior, thermochemical processing, and modeling of impurity effects in high-efficiency devices. The results of that effort are described in the following sections.

3. TECHNICAL PROGRESS

3.1 Crystal Growth and Analysis

3.1.1 Ingot Preparation

Growth of high-resistivity ingots for detailed evaluation of impurity behavior and electrical activity was the chief crystal growth activity recently. By JPL direction these studies will supplant some of the experimental silicon materials evaluation originally planned.

The six metal impurity-doped ingots completed this quarter for solar cell characterization are listed in Table 1. Four of the ingots, those for detailed analysis, were high-resistivity (30 ohm-cm) with three phosphorus doped and the fourth containing boron. The remaining two ingots to be used for high-efficiency studies were boron doped to a resistivity of 4 ohm-cm.

Each ingot's intentionally added metal impurity, associated crystalline structure, and task are indicated in the Table. All ingots were prepared by the Czochralski crystal growth method with details of the crystal growth equipment and conditions given in earlier reports.[1,2]

TABLE 1 INGOT IMPURITY, STRUCTURE AND TASK

Impurity	Structure	Task
Ti (30 ohm-cm)	Single	Material Evaluation
Cr (4 ohm-cm)	"	High Efficiency
Mo (4 ohm-cm)	"	"
V (30 ohm-cm)	"	Material Evaluation
Mo (30 ohm-cm)	"	"
Cr (30 ohm-cm)	"	"

TABLE 2. INGOT IMPURITY CONCENTRATION

Ingot Identification	Target Concentration $x10^{15}$ atoms/cm^3	Calculated Concentration $x10^{15}$ atoms/cm^3	Mass Spec. Analysis $x10^{15}$ atoms/cm^3
W-198-00-000	None	N/A	None
W-199-00-000	None	N/A	None
W-200-V-004-Poly	0.4	0.38	18.5*
W-201-Mo-007-Poly	0.005	0.003	77*
W-202-Ti-013-Poly	0.02	0.018	<0.25
W-203-V-005-Poly	0.04	0.053	<0.15
W-204-Cr-008-Poly	1.0	0.82	1322*
W-205-Fe-009-Poly	0.5	0.61	<1.5
W-206-V-006	0.02	0.026	<0.15
W-207-Mo-008	0.002	0.002	<0.5
W-208-Cr-009	0.2	0.19	0.6
W-209-Ti-014	0.02	0.024	<0.25
W-210-Ti-015	0.08	0.10	<0.25
W-211-Cu-007	1.0	1.0	2.6
W-212-Cu-008	10	12.5	27
W-213-Pb-001	Max. Conc.	Non Detectable	<0.10+
W-214-V-007-Poly	0.20	0.30	0.55**
W-215-Mo-009-Poly	0.0025	0.002	<0.5**
W-216-Cr-010-Poly	1.1	0.64	2.2**
W-217-Ta-005	0.00015	0.0003	<0.5
W-218-Ta-006	0.000065	0.0001	<0.5
W-219-V-008	0.007	0.009	<0.15
W-220-W-005	0.0008	0.0007	<0.15
W-221-Ni-005	10	8.2	<1.5

TABLE 2. INGOT IMPURITY CONCENTRATION (continued)

Ingot Identification	Target Concentration $x10^{15}$ atoms/cm^3	Calculated Concentration $x10^{15}$ atoms/cm^3	Mass Spec. Analysis $x10^{15}$ atoms/cm^3
W-222-Ag-002	4.5	3.2	6.0
W-223-Ni-006	1.0	1.1	<1.5
W-224-HSC/DCS057	NA++	None	<0.2+++
W-225-Mn-009	1.0	1.5	5.5
W-226-Mn-010	4.0	***	***
W-227-Cr-011-Poly	0.55	0.43	2.2
W-228-Gd-001	<0.2	++++	<0.2
W-229-Au-001	0.6	0.6	0.55
W-230-Al-003	120	64	120
W-231-Mn-011	0.25	0.23	0.75
W-232-N/Ti-001	0.02	0.01	<0.25****
W-233-Cr-012	0.11	0.12	0.2
W-234-Mo-010	0.0007	0.00051	<0.5
W-235-N/V-001	0.006	Processing	<0.15****
W-236-N/Mo-001	0.003	Processing	<0.5****
W-237-Cr-001	0.02	Processing	<0.15****

* Ingots contain metal-rich inclusions due to constitutional supercooling.
** Ingots regrown to remove metal-rich inclusions due to constitutional supercooling.
\+ Pb dopant vaporized on two separate ingot growths.
++ No intentional impurity
+++ Heavy metals < sensitivity of SSMS.
*** Single growth prohibited due to excessive impurity doping for permanence studies
++++ Atomic absorption analysis of ingot melt sample showed 2.8% Cd by weight of sample.
**** High resistivity ingot. 30 ohm-cm.

TABLE 3. BEST ESTIMATE OF IMPURITY CONCENTRATIONS

Ingot Identification	Best Estimate of Impurity Conc. ($\times 10^{15}$ ATOMS/CM^3)
W-198-00-000	NA*
W-199-00-000	NA
W-200-V-004-Poly	0.38
W-201-Mo-007-Poly	0.003
W-202-Ti-013-Poly	0.018
W-203-V-005-Poly	0.05
W-204-Cr-008-Poly	0.82
W-205-Fe-009-Poly	0.61
W-206-V-006	0.026
W-207-Mo-008	0.002
W-208-Cr-009	0.19
W-209-Ti-014	0.02
W-210-Ti-015	0.10
W-211-Cu-007	1.8
W-212-Cu-008	12.5
W-213-Pb-001	<0.1
W-214-V-007-Poly	0.4
W-215-Mo-009-Poly	0.002
W-216-Cr-010-Poly	1.0
W-217-Ta-005	0.0003
W-218-Ta-006	0.0001
W-219-V-008	0.009
W-220-W-005	0.0007
W-221-Ni-005	8.2

TABLE 3. BEST ESTIMATE OF IMPURITY CONCENTRATIONS (Continued)

Ingot Identification	Best Estimate of Impurity Conc. ($\times 10^{15}$ ATOMS/CM^3)
W-222-Ag-002	4.6
W-223-Ni-006	1.1
W-224-HSC/DCS057	++
W-225-Mn-009	1.5
W-226-Mn-010	***
W-227-Cr-011-Poly	0.4
W-228-Gd-001	<0.4
W-229-Au-001	0.6
W-230-Al-003	120
W-231-Mn-011-Poly	0.23
W-232-N/Ti-001	0.01****
W-233-Cr-012	0.12
W-234-Mo-010	0.0005
W-235-N/V-001	0.006****
W-236-N/Mo-001	0.003****
W-237-Cr-001	0.02****

* Not applicable
++ No intentional impurity
*** Single growth prohibited due to excessive impurity doping for permanence studies
**** High resistivity ingot. 30 ohm-cm

TABLE 4. INGOT ELECTRICAL AND DEFECT CHARACTERISTICS

Ingot Identification	TGT Resistivity (ohm-cm)	Actual Resistivity (ohm-cm)	Etch Pit Density (/cm^2)
W-198-00-000	4.0	4.1-3.9	0-3K
W-199-00-000	4.0	3.7-3.5	1-5K
W-200-V-004/Poly	4.0	3.6-2.3	NA*
W-201-Mo-007/Poly	4.0	3.8-2.3	NA
W-202-Ti-013/Poly	4.0	5.3-3.9	NA
W-203-V-005/Poly	4.0	4.4-3.8	NA
W-204-Cr-008/Poly	4.0	4.7-4.3	NA
W-205-Fe-009/Poly	4.0	4.0-3.2	NA
W-206-V-006	4.0	3.7-3.6	0-5K
W-207-Mo-008	4.0	3.8-3.5	0-15K
W-208-Cr-009	4.0	3.7-3.5	0-15K
W-209-Ti-014	4.0	4.0-3.3	0-10K
W-210-Ti-015	4.0	4.0-3.5	0-5K
W-211-Cu-007	4.0	4.0-3.1	0-5K
W-212-Cu-008	4.0	3.9-3.3	5-20K
W-213-Pb-001	4.0	3.3-2.7	10-20K
W-214-V-007-Poly	4.0	3.8-3.1	NA
W-215-Mo-009-Poly	4.0	3.8-1.7	NA
W-216-Cr-010-Poly	4.0	7.6-2.9	NA
W-217-Ta-005	4.0	3.5-3.0	0-10K
W-218-Ta-006	4.0	3.7-3.2	0-5K

TABLE 4. INGOT ELECTRICAL AND DEFECT CHARACTERISTICS (Continued)

Ingot Identification	TGT Resistivity (ohm-cm)	Actual Resistivity (ohm-cm)	Etch Pit Density (/cm^2)
W-219-V-008	4.0	3.6-3.3	0-5K
W-220-W-005	4.0	3.7-3.2	0.20K
W-221-Ni-005	4.0	3.5-3.1	OK
W-222-Ag-002	4.0	5.8-5.7	0-Gross Lineage
W-223-Ni-006	4.0	3.6-3.1	0-5K
W-224-HSC/DCS057	1.0	1.4-1.2	5-20K
W-225-Mn-009	4.0	5.5-3.5	0-5K
W-226-Mn-010	4.0	***	***
W-227-Cr-011-Poly	4.0	3.9-3.5	NA
W-228-Gd-001	4.0	5.4-5.1	0-Gross Lineage
W-229-Au-001	4.0	4.3-4.2	0-30K
W-230-Al-003	1.5	1.5-0.5	0-20K
W-231-Mn-011-Poly	4.0	4.4-3.1	NA
W-232-N/Ti-001	30	31-23	0-20K
W-233-Cr-012	4.0	4.1-3.7	0-5K
W-234-Mo-010	4.0	4.1-3.8	0-5K
W-235-N/V-001	30	33.5-23.0	0-5K
W-236-N/Mo-001	30	34.4-28.3	0-20K
W-237-Cr-001	30	24.0-17.4	0-5K

* Not applicable
*** Single growth prohibited due to excessive impurity doping for permanence studies

TABLE 5. INGOT CARBON AND OXYGEN CONCENTRATIONS

Ingot Identification	Carbon Concentration ($X10^{16}$ atoms/cm^3)	Oxygen Concentration ($X10^{16}$ atoms/cm^3)
W-201-Mo-007-Poly	7.0	61
W-203-V-005-Poly	12	59
W-205-Fe-009-Poly	8.0	34
W-207-Mo-008	5.4	43
W-209-Ti-014	6.4	61
W-211-Cu-007	6.0	57
W-213-Pb-001	8.0	57
W-215-Mo-009-Poly	10.0	56
W-217-Ta-005	12.0	50
W-219-V-008	25.0	43
W-221-Ni-005	10.0	53
W-223-Ni-006	20.0	77
W-225-Mn-009	4.0	58
W-227-Cr-011-Poly	16.0	82
W-229-Au-001	7.3	80
W-231-Mn-011-Poly	13.0	38
W-233-Cr-012	9.0	45
W-235-N/V-001	12.0	50
W-237-Cr-001	8.0	55

3.1.2 Ingot Evaluation

The data listed in Table 2 provide a detailed description of the measured and calculated impurity concentrations of all Phase IV ingots. The calculated value is based on the melt impurity concentration determined by atomic absorption analysis and the known segregation coefficients of the contaminants.[6] The measured impurity concentration is that determined by spark source mass spectroscopy[2,3] on seed and samples from each ingot.

A best estimate[3] of the impurity concentrations for each Phase IV ingot is listed in Table 3. The best estimate for ingot W228-Gd is less than 2×10^{14} atoms/cm^3. Neutron activation analysis in progress on W228 samples is expected to improve on this best estimate.

The resistivity and etch pit data for all of Phase IV ingots are compiled in Table 4. This analysis is not applicable to the polycrystalline samples.

Carbon and oxygen concentrations of each odd-numbered ingot were measured by Fourier Transform Infrared Spectroscopy at room temperature; see Table 5. The amplitude of the absorption peaks at 605 cm^{-1} and 1107 cm^{-1} is proportional to the carbon and oxygen concentrations, respectively. The calibration factors used in these evaluations are 2.2 atoms/cm^2 for carbon[2] and 4.9 atoms/cm^2 for oxygen[4]. Normal carbon and oxygen concentrations found in Czochralski-grown material are in the range of 2.5 to 5×10^{17} atoms/cm^3 for carbon and 5 to 150×10^{16} atoms/cm^3 for oxygen.

3.1.3 Impurity-induced Structural Breakdown

A characteristic of silicon ingots grown from heavily doped melts is crystal structure breakdown which can be attributed to constitutional supercooling of the melt at the crystal-liquid interface.[6] This breakdown of crystalline structure manifests itself by the appearance of a feathered pattern on the crystal surface and by impurity-rich inclusions in the interior of the ingot.

For a given crystal growth rate, ingot diameter, and imposed thermal gradient, the onset of impurity-induced structural degradation occurs at a critical liquid-impurity concentration termed C_ℓ^*. In single crystal experiments where growth rates of 6.5-8cm/hr and ingot diameters of 3 3 to 4cm are typical, C_ℓ^* has ranged from 1 to 5 x 10^{20} cm^{-3} for the metal impurities investigated.

During Phase IV several purposely polycrystalline ingots have been grown and contaminated with various impurities in order to evaluate impurity-grain boundary interactions. These ingots were nucleated from seeds having several 0.5 to 1mm-sized grains; the polycrystalline structure propagated the length of the ingot. For the most heavily doped melts these ingots also underwent impurity-induced structural degradation: metal rich inclusions formed within the grains, eutectic material formed at the grain boundaries, and the grain size abruptly diminished to a fine network of twins and grain boundaries well below the 1mm diameters originally present.

For three impurities examined so far—V, Mo and Cr—the threshold for structural degradation is smaller in polycrystalline ingots than in silicon single crystals grown under comparable conditions; see Table 6. The greatest difference in behavior occurs for V where C_ℓ^* for the polycrystalline ingot is more than an order of magnitude smaller for the polycrystalline ingot than for the single crystal.

Our single crystals are grown in the [111] direction so the crystal-liquid interface is a (111) facet. Such singular faces stabilize a planar solid-liquid interface against constitutionally induced breakdown. Thus, one might expect structural breakdown to occur at lower values of C_ℓ^* in polycrystals which contain a multiplicity of growth orientations, as well as grain boundaries which perturb an otherwise smooth solid-liquid interface and are thus favored sites to initiate breakdown.

Besides the information on breakdown in polycrystalline ingots, we have compiled an up-to-date set of data for single crystals as well; see Table 7. We have noted before[2,6] that the critical impurity concentration for breakdown can be estimated from a relation of the form

TABLE 6

COMPARISON OF CRITICAL IMPURITY CONCENTRATIONS FOR STRUCTURAL BREAKDOWN IN SINGLE AND POLYCRYSTALLINE INGOTS

Ingot	Impurity	Measured Breakdown Concentration C_ℓ^*, 10^{20} cm^{-3}
W009	V	2.4
W203-Poly+	V	0.15
W139	Mo	1.3
W201-Poly+	Mo	0.9
W004	Cr	3.6
W216-Poly+	Cr	1.5

+ nucleated from a polycrystalline seed

TABLE 7

DIFFUSION CONSTANTS FOR METALS IN LIQUID SILICON CALCULATED FROM INGOT BREAKDOWN DATA

Ingot	Impurity	$C_\ell^*(10^{20}cm^{-3})$	$D_{calc}(10^{-4}cm^2/sec)$
W228	Gd	1.8	1.51
W	Zr	1.5	1.80
W145	W	1.2	1.88
W139	Mo	1.3	1.96
W009	V	2.4	2.04
W140	Ti	1.7	2.00
W143	Ti	1.7	2.27
W137	Ti	1.7	2.37
W166	Fe	1.9	2.41
W173	Fe	1.9	2.46
W135	Fe	2.1	2.55
W146	Co	2.1	2.55
W184	Pd	3.0	2.56
W222	Ag	3.0	2.60
Ref. 8	Cu	0.7	4.20

$$C_\ell^* = -\frac{D}{m}\left[\frac{A}{r^{1/2}R} - B\right]e^{-\frac{R\delta}{D}} \qquad (1)$$

where m is the phase diagram liquidus slope, D the liquid diffusion constant of the impurity (cm^2/sec), r the crystal radius (cm), R the growth rate (cm/sec), and δ the thickness of the diffusion-controlled impurity boundary layer at the crystal interface (cm). A and B are derived from system thermal and material constants.[2]

With a suitable value for δ, it is possible then to estimate the magnitude of D from the measured value of C_ℓ^* for a given impurity. In previous analyses we assumed $D = 10^{-4}$ cm^2/sec, a typical value for metals in liquid silicon.[7] The good agreement between measured and calculated values of C_ℓ^* indicated this was a fair choice.

Since then we have made a preliminary estimate of D for many of the impurities studied in an effort to discover whether any periodic trends in D occur with impurity chemistry or atomic size.[6] To accomplish this we reformulate equation (1) by employing the relation

$$\frac{\delta}{D} = 1.6D^{-2/3}v^{1/6}w^{-1/2} \text{ to eliminate } \delta.$$

Using $v = .0106$ cm/sec for kinematic viscosity[7] and $w = 0.167s^{-1}$ for the rotation rate we obtain $\delta/D = 1.8D^{-2/3}$.

Substituting in (1) and introducing numerical constants[2,6] gives

$$C_\ell^* = 1.07(10^{20})De^{-1.8RD^{-2/3}}\left[\frac{92.44}{r^{1/2}R} - 6.88(10^3)\right] \qquad (2)$$

We introduced sets of data(C_ℓ^*, r and R) for each impurity into (2) and solved for D interactively with a programmable hand calculator. The results compiled in Table 7 indicate values of D ranging from 1.51 to 4.2×10^{-4} cm^2/sec for the impurities. We caution that these values cannot be exact owing to imprecision in numerical constants, the simple thermal model we used, and the error in precisely identifying the initiation of breakdown. However, relative comparisons should be quite good.

3.2 The Permanence of Impurity Effects in Silicon Solar Cells

3.2.1 Mechanism of High-Temperature Aging

We have previously shown that solar cell performance is a function of material quality and device process history.[1-3] Aging of cell performance due to impurities is species and temperature dependent. Since projected solar cell operating times (>20 years) are long compared to practical test times, we extrapolated from accelerated aging tests to estimate long-term solar cell performance.[3]

While time-temperature data can be used to provide a phenomenological model for cell aging, the data shed little light on the mechanism of performance degradation. Recently, we have employed deep level spectroscopy (DLTS) coupled with detailed I-V analysis[3] to investigate these mechanisms for two impurities, Ag and Cr. Highlights of our preliminary results are given below.

DLTS measurements were performed after the aging treatment by subdividing the solar cell mesa into 30-mil diameter mesa diodes with Ti-Au contact. DLTS measurements were also performed at a location 5μm below the solar cell junction by fabricating 30-mil diameter Ti-Au Schottky barrier diodes on the p-base of the solar cell after the solar cell junction was etched off.

In Table 8 we show the solar cell data before and after the aging treatment on the Cr and Ag samples. In Table 9 are the DLTS results on the corresponding samples. Solar cell data from Ingot 222-Ag (sample No. 32) indicate that after ten hours of aging the cell at 400°C there was some loss in OCD lifetime. This is also reflected by the decrease in I_{SC} and V_{OC} after aging. Figure 1 is the dark I-V plot of the Ag-doped cell before and after the aging treatment. The transformed I-V curves indicate that the junction response (lower segment) is not appreciably affected and cannot account for the observed degradation. The shift in the upper segment confirms the observed loss in carrier lifetime.

TABLE 8

CELL DATA FOR Ag AND Cr-DOPED SOLAR CELLS
EMPLOYED IN AGING TESTS

Ingot ID	Aging Treatment In N_2 Ambient	I_{SC}	V_{OC}	FF	η	τ_{OCD}
222-Ag, #32	None	20.99	.524	.717	8.36	1.71
222-Ag, #32	400°C/10 hrs.	19.30	.515	.681	7.16	0.78
072-Cr, #25	None	20.86	.491	.696	7.93	1.79
072-Cr, #25	600°C/1 hr.	19.80	.534	.731	8.17	1.30
072-Cr, #43	800°C/100 hrs.	14.80	.480	.667	5.01	0.91

TABLE 9

DLTS RESULTS AFTER AGING TREATMENTS (N_2 ATMOSPHERE) PERFORMED ON Ag AND Cr-DOPED SAMPLES

Ingot ID	Aging Treatment	Trap Level (eV)	Trap Concentration (cm^{-3})
222-Ag, #32	None	None	-
222-Ag, #32 (in the junction)	400°C/10 hrs.	E_V+0.43	5.3×10^{12}
222-Ag, #32 (5 μm below the junction)	400°C/10 hrs.	None	-
072-Cr, #25	None	None	-
072-Cr, #25 (in the junction)	600°C/1 hr.	None	-
072-Cr, #25 (5 μm below the junction)	600°C/1 hr.	None	-
072-Cr, #6 (in the junction)	200°C/225 hrs.	None	-
072-Cr, #6 (5 μm below the junction)	200°C/225 hrs.	None	-
072-Cr, #43 (in the junction)	800°C/100 hrs.	E_V+0.30	1×10^{13}
072-Cr, #43	800°C/100 hrs.	E_V+0.30	2.8×10^{12}

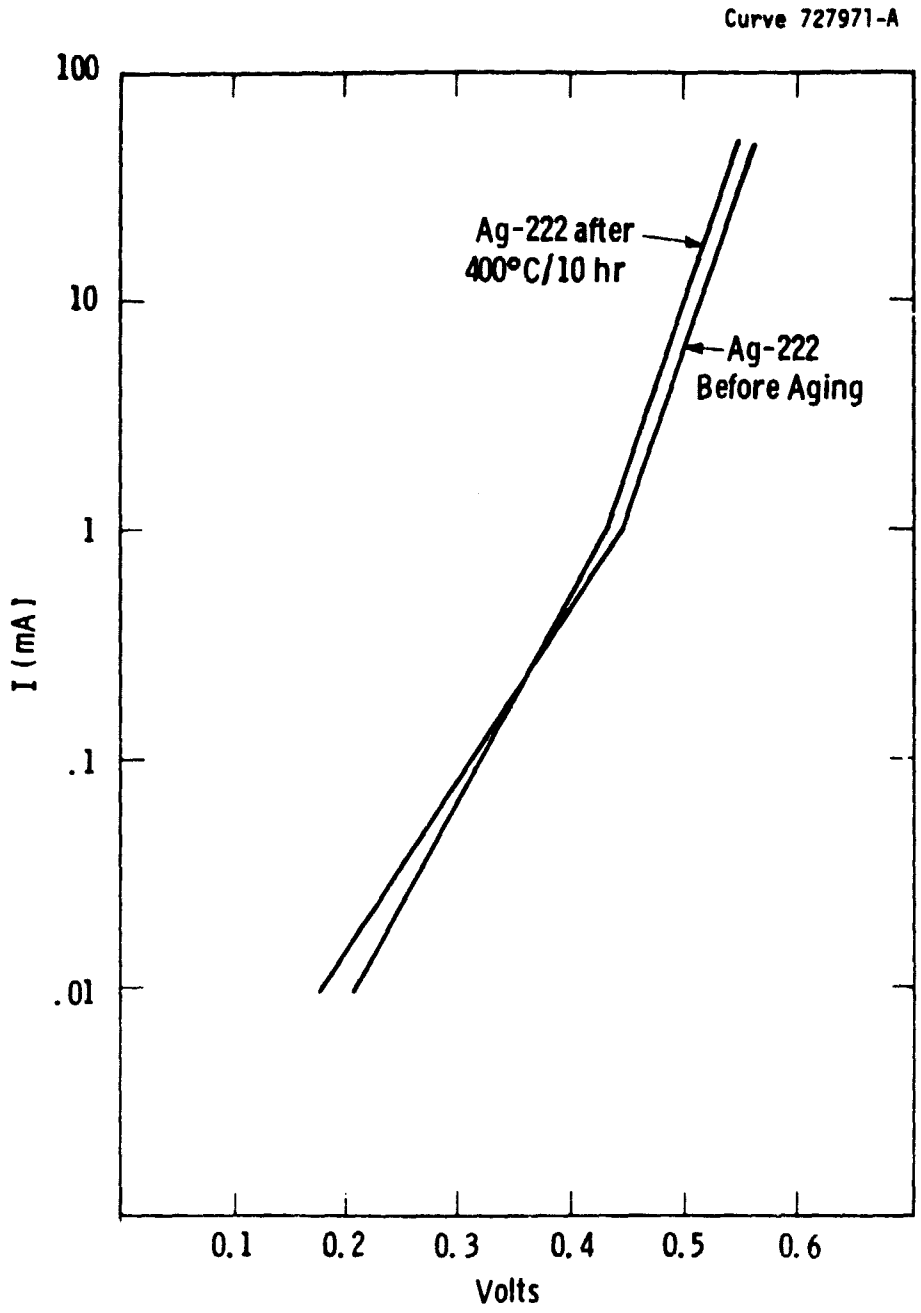

Figure 1 Transformed I-V Curves for Ag-Doped Solar Cells Before and After Aging 10 Hours at 400°C.

In Table 9 the data indicate that prior to the 10 hour, 400°C aging treatment no deep level was detected in the cell; following aging of the Ag-doped cell we did observe a deep level at E_V+0.43eV. The concentration of this level near the junction was 5.3×10^{12} cm^{-3}, but 5μm below the junction region the level was undetectable. Since more than 70% of solar radiation is absorbed within the first 10μm of the cell, this trap center detected near the junction could be responsible for the observed decrease in cell efficiency and the carrier lifetime.

It is difficult to determine the precise source of this center, but the literature[9] indicates that Ag in silicon gives rise to a deep level at E_V+0.45eV. At this point we can only speculate that the majority of the Ag atoms present in the starting wafer are electrically inactive and thus cannot be detected by the DLTS technique. Aging for a prolonged time at elevated temperatures may equilibrate or redistribute the Ag into a new phase, or site, where it behaves as a trap center. (The silicon ingot may cool too rapidly following crystal growth for the equilibrium redistribution of impurities to occur by diffusion. Our earlier finding that electrically active impurity concentration is only a fraction of total metallurgical impurity concentration suggest that all the impurity atoms are not on equivalent sites).

At present we have no explanation why the trap level was not detected 5μm below the cell junction; these are preliminary results on a single sample which require confirmation.

The data in Table 8 also show that aging of a Cr-contaminated solar cell at 600°C for 1 hour in N_2 does not appreciably alter the cell performance. Following 100 hours at 800°C, however, aging caused almost a 3% degradation in the (absolute) cell performance. Cell data indicate that this is primarily due to the reduction in carrier lifetime since I_{SC} and V_{OC} both are substantially reduced.

It is noteworthy that the high-temperature annealing for Cr samples was performed on the starting wafer prior to cell fabrication. The DLTS data in Table 9 indicate that no Cr-induced trap centers were

detected in the cells before aging or after the one-hour treatment at 600°C. This is consistent with our observation that no appreciable change in the cell efficiency took place. However, after the 100-hour 800°C treatment in N_2 and subsequent cell fabrication, we found a deep level at E_V+0.30eV. Its concentration in the junction was 1 x 10^{13} cm^{-3}, diminishing to 2.8 x 10^{12} cm^{-3} at 5μm below the junction. We note that this level does not correspond to the levels (E_V+0.22 and E_V+0.31) observed[10] in the as-grown Cr-contaminated wafers. Although the energy of this center is very close to E_V+0.31eV in the DLTS spectra, the peak occurs at a different temperature, indicating different capture cross section. In order to show that this center is related to the Cr impurity, we must look at an uncontaminated base line wafer treated similarly. We plan to carry out such experiments and verify these preliminary results in the future.

Aging-induced degradation in these cell performances appears to be due to the loss of carrier lifetime via newly formed deep levels. Since N_2 annealing of Ag and Cr contaminated samples showed different levels, one might speculate from these extremely limited data that the aging-induced centers might be related to respective impurity rather than to thermal or ambient-induced lattice defects.

3.2.2 Electrical Bias Effects

We have been conducting a series of tests to deduce empirically any interactions between electric fields and impurities in silicon solar cells. To perform these experiments, base line cells and cells containing one of several representative impurities are operated under 30-mA/cm^2 bias. The cells are run at elevated temperature to accelerate any interactions which may occur. Ingots employed in the experiments are listed in Table 10.

Solar cell operation for periods of 100 hours have now been carried out at eleven different test temperatures. We plan to continue these tests at increasingly higher temperatures until clear evidence of cell efficiency degradation is observed. The status of the experiment is outlined below.

TABLE 10

SILICON INGOTS UNDERGOING ELECTRICAL BIAS SOLAR CELL TESTING

Ingot No.	Impurity
W-198-00-000 Baseline	None
W-166-Fe-007	Fe 1.06×10^{15}
W-167-Nb-001	Nb $<0.044 \times 10^{15}$
W-192-Ag-001	Ag 2.20×10^{15}
W-181-Cr-006	Cr 1.04×10^{15}
W-106-Fe-001	Fe 0.4×10^{15}
W-056-Cu-005	Cu 65×10^{15}
W-183-Nb-002	Nb $<0.009 \times 10^{15}$
*W-123-Ti-008	Ti 0.105×10^{15}

*These samples were broken after the 225° test.

Average relative cell efficiency of the base line (no intentional impurity) cells after each temperature-bias exposure is plotted in Figure 2. This represents cell degradation which is attributable to effects other than specific impurity effects. Updated curves showing the average relative cell efficiencies of the impurity-doped cells (normalized to the base line cell behavior) are shown in Figures 3 to 9.

Clearly, the degradation at temperatures up to 245°C is small, usually less than 10%. As in earlier results no systematic effect is observable; tests are continuing at higher temperatures.

3.3 Thermochemical Processing

3.3.1 Ion Implant-Induced Damage Gettering

Various thermochemical processes can be performed on silicon, subsequent to silicon crystal growth, in order to mitigate the harmful effects of any metal contamination present. The thermochemical processes studied during this program have been (1) $POCl_3$ gettering, (2) HCl gettering, and (3) damage gettering.[3,11] It was previously observed[11] that damage gettering by a lapped surface on the back side of solar cell wafers was not effective in enhancing the effect of HCl gettering. Because the damage induced by back surface lapping is both difficult to quantify and to reproduce accurately, a more easily controlled damage method, back surface ion implant damage, was chosen for further investigation.

Two impurities, copper and titanium, representative of fast and slowly diffusing elements in silicon, were made the test vehicles for these studies.

3.3.1.1 Experimental Sequence

Wafers containing the two impurities were damaged on their back sides by argon ion implantation. The ions were implanted at 100 keV to a dose level of 1×10^{15} cm^{-2}. Some wafers were simply annealed at 1100°C in nitrogen to assess the gettering capability of back surface damage alone; others were further gettered with HCl at 1000°C and 1100°C, or with

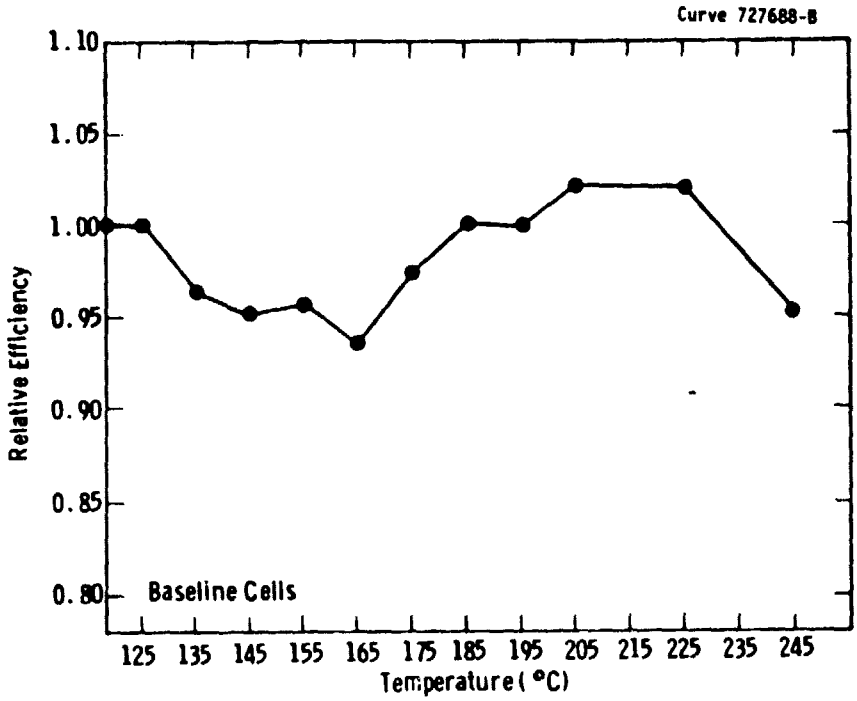

Figure 2 Effect of electrical bias on relative efficiency as a function of stress temperature-base line cells.

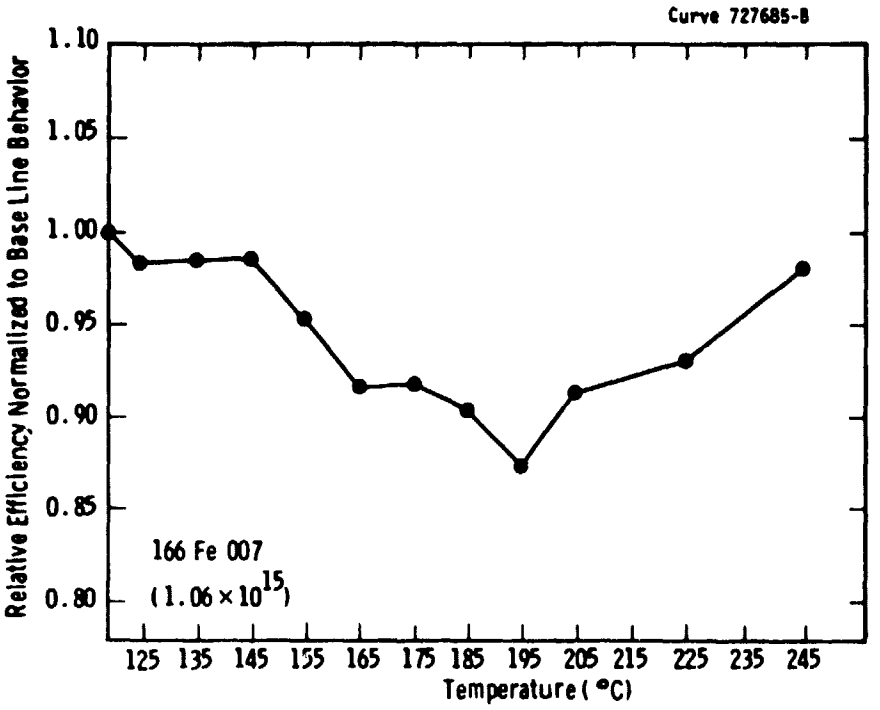

Figure 3 Effect of electrical bias on relative efficiency as a function of stress temperature-Fe-doped (1.06×10^{15} cm^{-3}) cells.

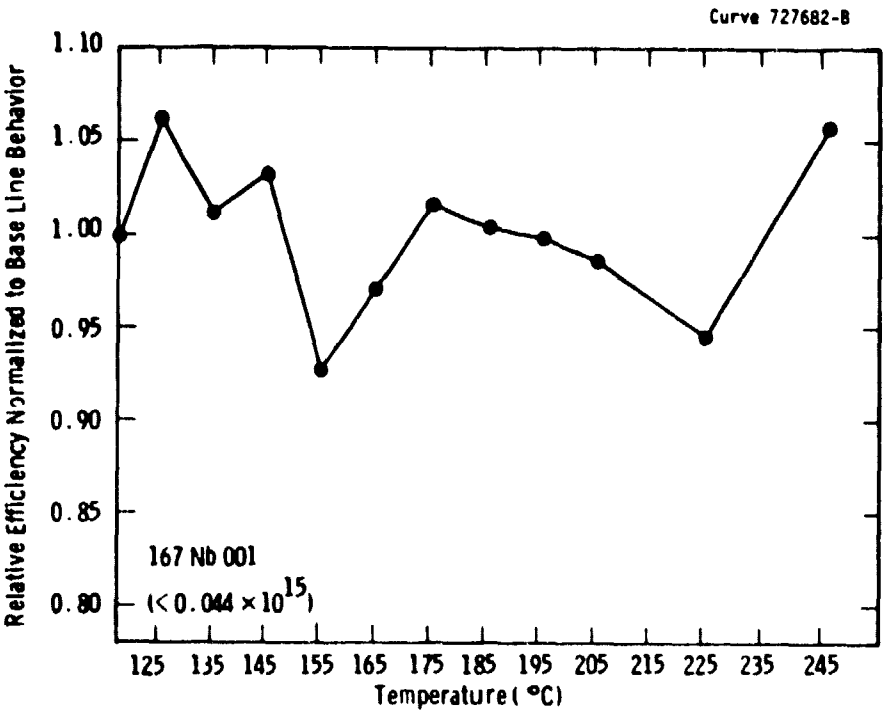

Figure 4 Effect of electrical bias on relative efficiency as a function of stress temperature-Nb-doped ($<0.44 \times 10^{15}$ cm^{-3}) cells.

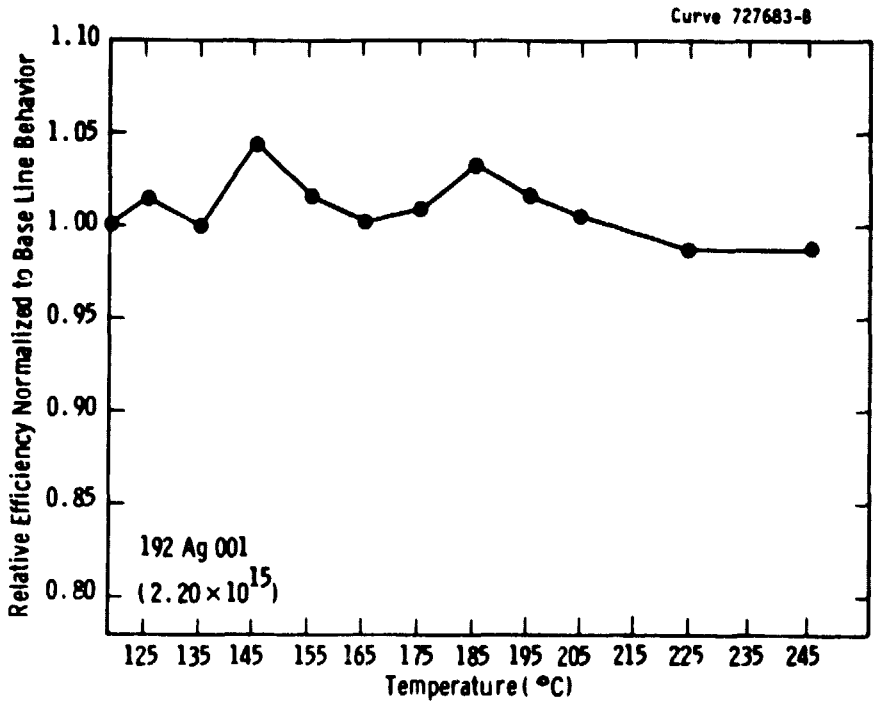

Figure 5 Effect of electrical bias on relative efficiency as a function of stress temperature-Ag-doped (2.20 x 10^{15} cm^{-3}) cells.

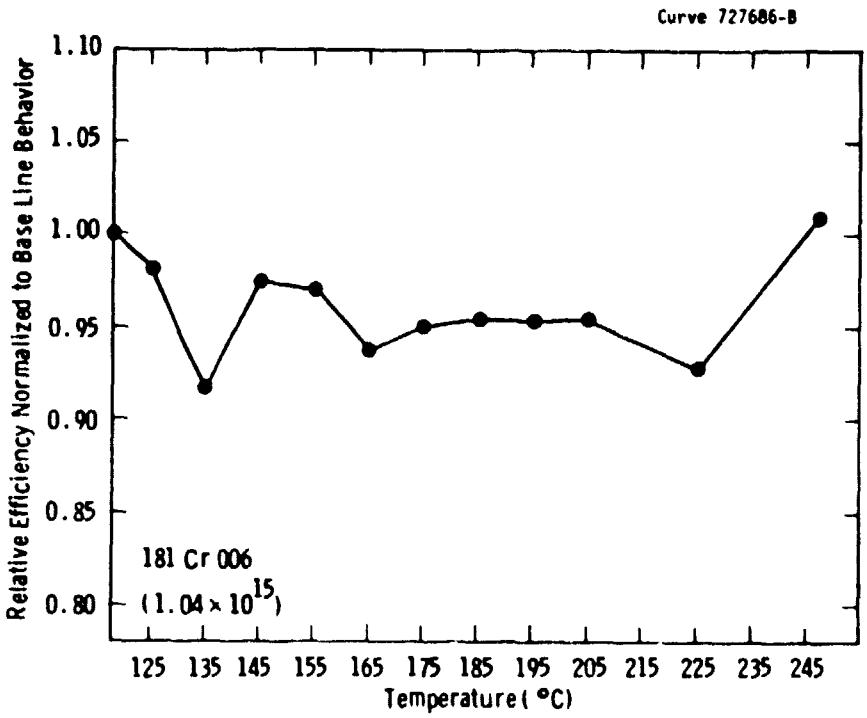

Figure 6 Effect of electrical bias on relative efficiency as a function of stress temperature-Cr-doped (1.04×10^{15} cm^{-3}) cells.

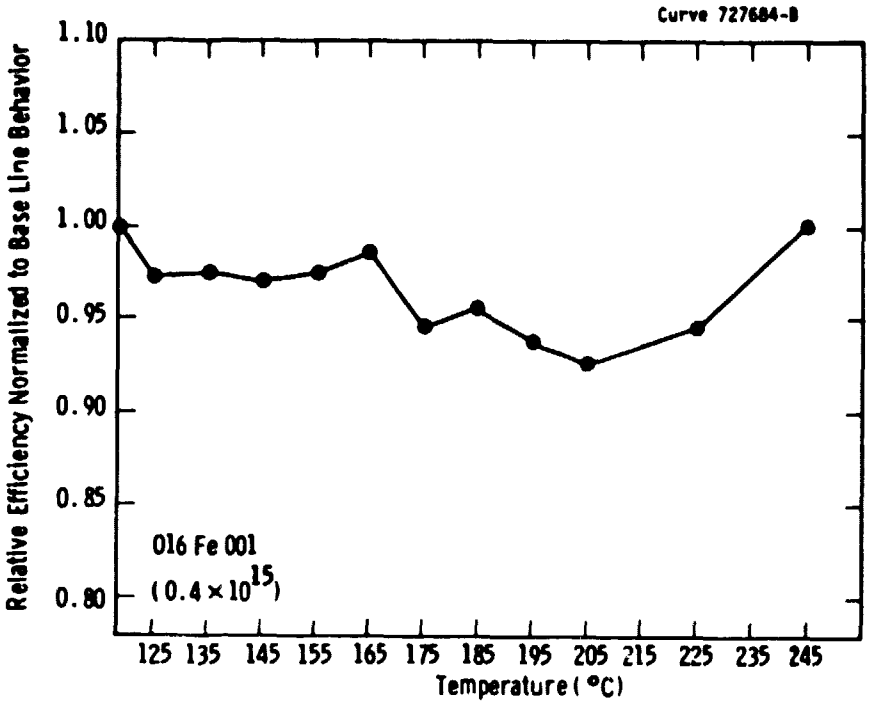

Figure 7 Effect of electrical bias on relative efficiency as a function of stress temperature-Fe-doped (0.4 x 10^{15} cm^{-3}) cells.

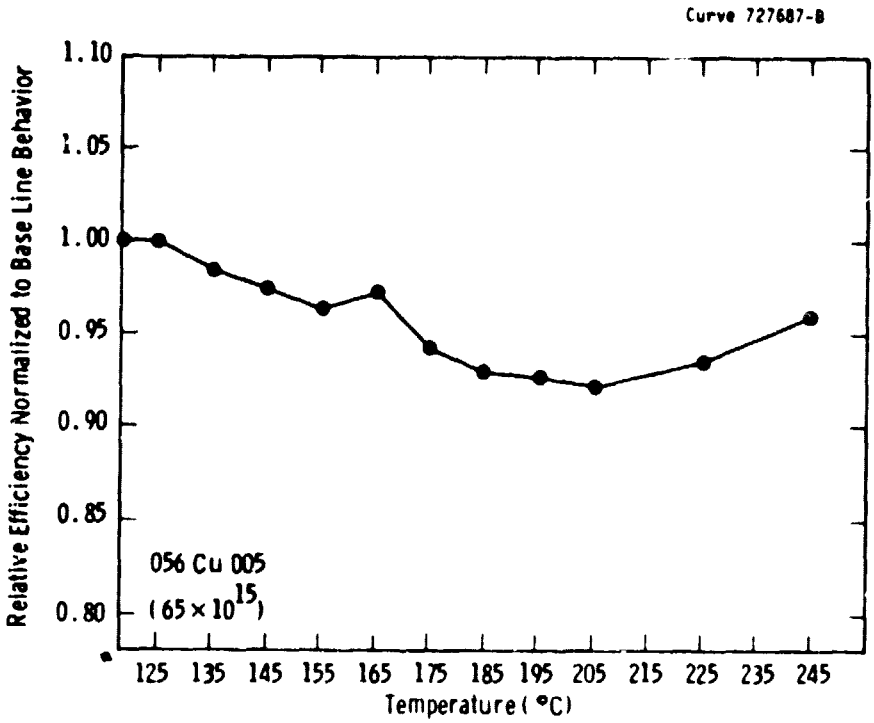

Figure 8 Effect of electrical bias on relative efficiency as a function of stress temperature-Cu-doped (65 x 10^{15} cm^{-3}) cells.

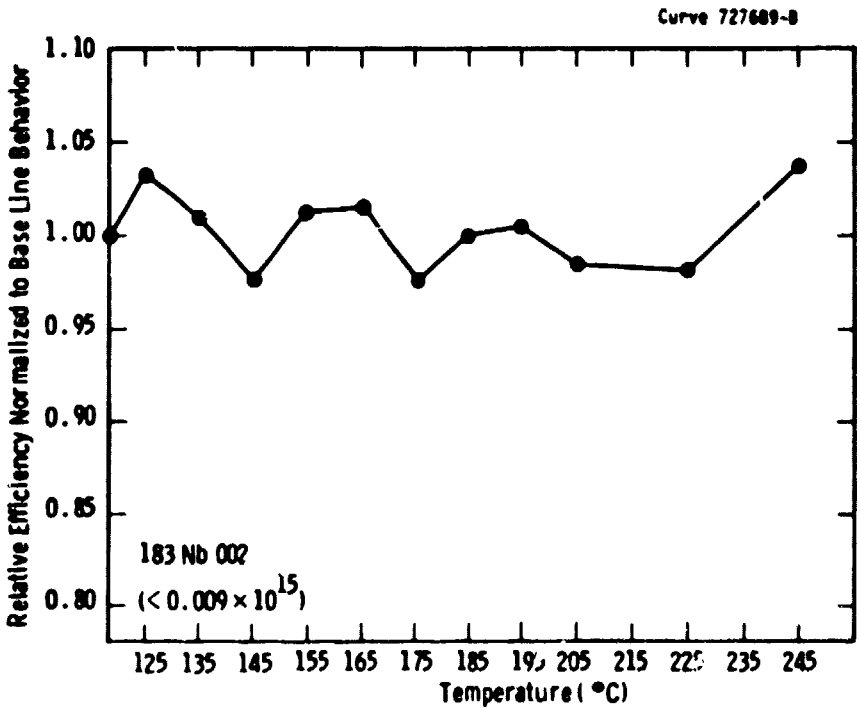

Figure 9 Effect of electrical bias on relative efficiency as a function of stress temperature-Nb-doped ($<0.009 \times 10^{15}$ cm^{-3}) cells.

$POCl_3$ at 950°C, 1000°C, and 1100°C. Gettering times were always for one hour. Following the thermochemical gettering step, the HCl-gettered wafers and the "damage only"-gettered wafers were processed to remove surface oxides. The $POCl_3$-gettered wafers were chemically etched to remove the phosphorus-doped surfaces formed during the gettering process. All wafers were then processed to form solar cells according to our standard process sequence.[3] The results of the experiment are depicted in Figures 10 through 13.

3.3.1.2 Gettering of Copper

Copper is known to diffuse rapidly through silicon.[3] In solar cells, its primary effect, unlike that of most heavy metals, is to cause efficiency degradation by increasing junction leakage rather than by reducing minority-carrier lifetime. The mechanism by which this degradation takes place is believed to be the precipitation of copper atoms at defect sites within the silicon, causing electric field concentrations in the junction region and occasionally shunting the junction with low-resistance paths. Thus, the effects of any high-temperature treatment of copper-containing silicon can be expected to be complex.

Figures 10 and 11 illustrate that copper-containing silicon as grown can be fabricated into solar cells whose efficiencies are very close to those of devices fabricated on pure silicon. A high-temperature process, such as ion damage gettering alone, decreases cell efficiency perhaps because it permits more copper precipitation to take place, while the ion-damaged region is not very effective in removing copper atoms from the junction region.

$POCl_3$ or HCl gettering, either alone or in combination with ion damage gettering, are more effective than is ion damage gettering alone, but on the basis of our data it is doubtful that any of these gettering processes can produce better material than the original as-grown silicon.

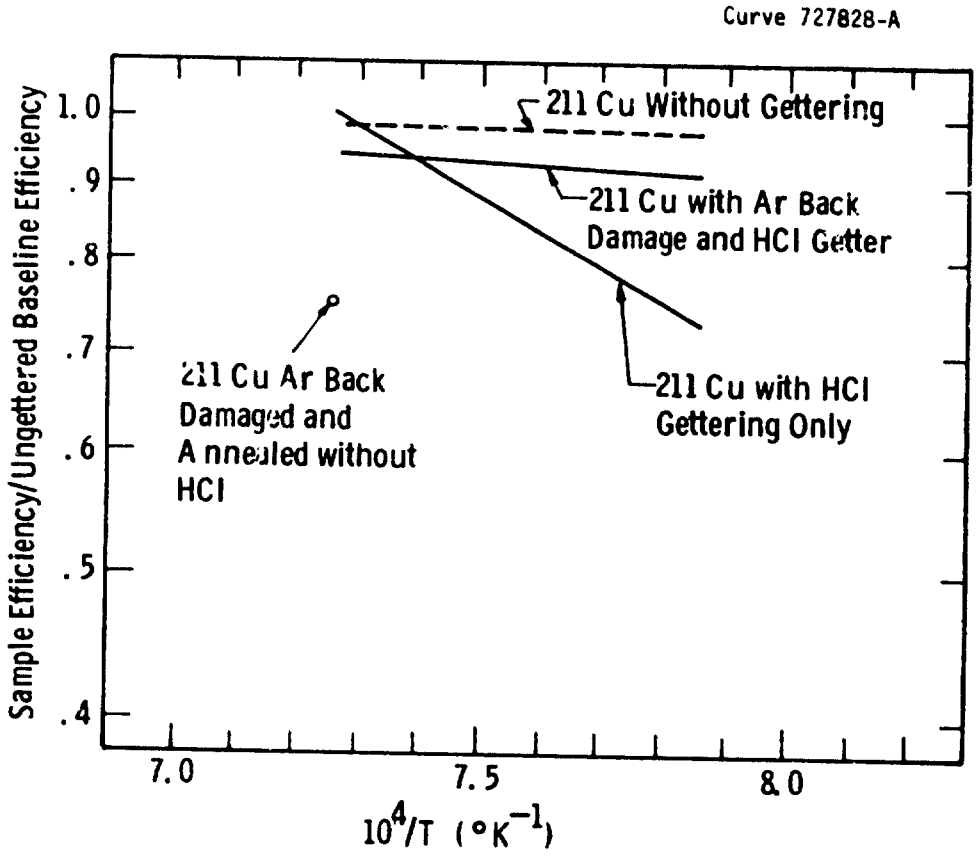

Figure 10 Effects of HCℓ and ion implant damage gettering on solar cell material containing copper.

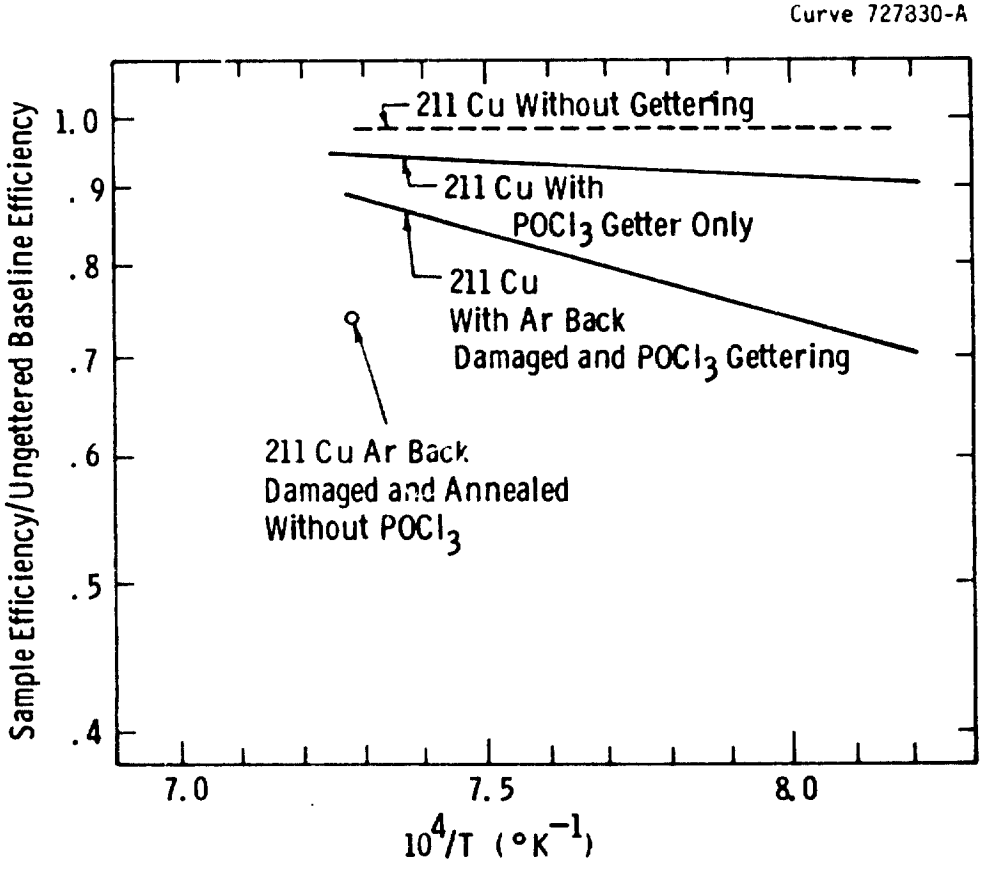

Figure 11 Effects of $POCl_3$ and ion implant damage gettering on solar cell material containing copper.

3.3.1.3 Gettering of Titanium

Titanium diffuses fairly slowly through silicon.[3] Its presence in silicon causes minority-carrier traps which reduce the lifetime in both n and p-type material. The data in Figures 12 and 13 show that ion damage gettering by itself is effective in raising the efficiencies of titanium-containing silicon solar cells. They also show that the improvement due to ion damage gettering is small in comparison to what can be achieved with HCℓ or $POCℓ_3$ gettering.

3.3.1.4 Conclusions

The data presented here show that, at least for copper and titanium impurities in silicon, ion implant damage gettering is not as effective for improving solar cell efficiency as are the HCℓ or $POCℓ_3$ treatments we have previously studied.[3] In the case of copper, high-temperature processing appears to degrade the material; the original quality of the material can be regained only by prolonged gettering at high temperature.

In contrast to the results for Cu, all of the treatments improved the efficiencies of the Ti-doped cells compared to the ungettered condition. Based on these and earlier results our conclusions are:

(1) $POCℓ_3$ and HCℓ gettering raise the solar cell efficiency by 1 to 1.5% (absolute) compared to the ungettered case; the improvement is greatest at the highest gettering temperature, 1100°C.

(2) The combined treatments, Ar damage plus HCℓ or $POCℓ_3$, also improve cell efficiency but not as much as HCℓ or $POCℓ_3$ alone.

(3) Ar damage plus annealing at 1100°C (no $POCℓ_3$ or HCℓ) produces a small but real improvement in cell efficiency compared to the untreated devices.

(4) The HCℓ-based treatments appear more effective overall than those employing $POCℓ_3$.

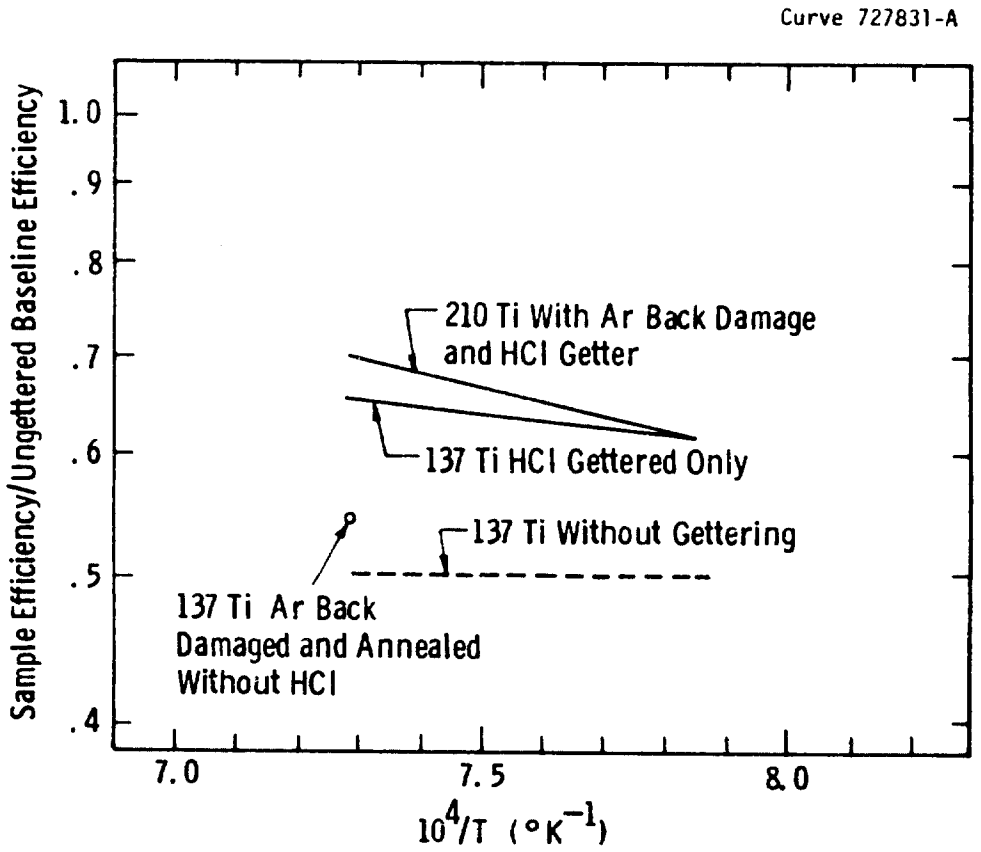

Figure 12 Effects of HCℓ and ion implant damage gettering on solar cell material containing titanium.

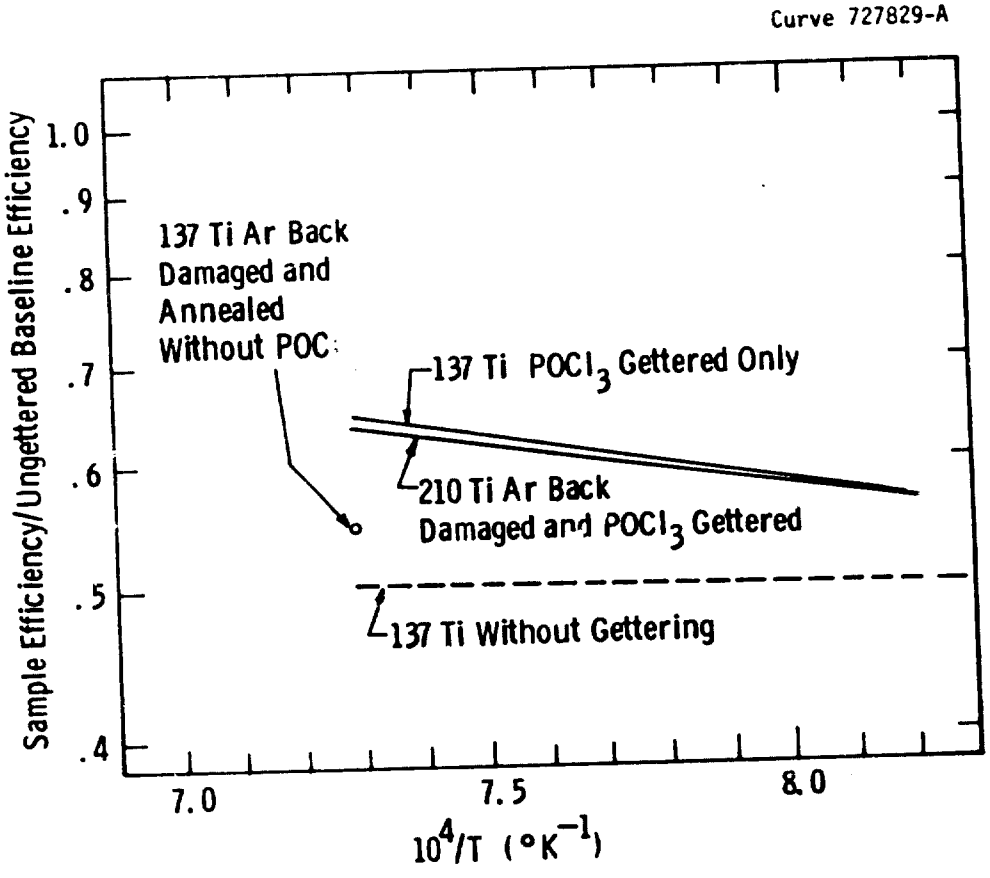

Figure 13 Effects of $POC\ell_3$ and ion implant damage gettering on solar cell material containing titanium.

3.3.2 Impurity Response to N_2 Heat Treatment

We reported earlier[3] that a 50-minute $POCl_3$ gettering (1) had no effect on Mo, (2) produced a composition profile in the first 10 μm near the silicon surface for Ti, and (3) had a significant impact on Cr (the electrically active concentration fell below the detection limit of DLTS technique). In order to determine whether the above effects were due to $POCl_3$ treatment or to the heat treatment alone, we annealed the metal-contaminated wafers in N_2 at 825°C for 50 min. without any $POCl_3$. (After heat treatment, 30-mil diameter Ti-Au Schottky barrier diodes were fabricated at various depths to detect active impurity concentration via deep level transient spectroscopy.)

The results of these experiments are shown in Figure 14. The electrically active impurity concentration in the Ingots Mo-77, Ti-123, and Cr-181 prior to treatment was 4×10^{12} cm^{-3}, 4×10^{13} cm^{-3} and 1×10^{14} cm^{-3}, respectively. The data show that, as observed in the case of $POCl_3$ treatment, N_2 treatment at 825°C/50 min. also resulted in a profile-like distribution for Ti, the Cr concentration was reduced below the detection limit, and there was no appreciable affect on Mo concentration.

In previous experiments the $POCl_3$ gettering of Ti was performed using ingot 137-Ti, instead of 123-Ti, in which the electrically active Ti concentration was 8×10^{13} cm^{-3}. After $POCl_3$ gettering of this ingot, the surface concentration was reduced to about 2×10^{13} cm^{-3}, and there was a Ti outdiffusion profile in the first 10 μm of the wafer surface. Results of the N_2 treatment of ingot Ti-123 appear to produce similar effects. However, in order to compare accurately the impact of $POCl_3$ and N_2 treatment on Ti, we must first complete the $POCl_3$ gettering on ingot Ti-123; these results will be quoted in the next report. We do note here that N_2 treatment alone produces a diffusion-like profile for Ti impurity. A possible explanation for this behavior could be that the surface, not mechanically damaged during treatment, may still provide low free energy sites or a sink for some impurities. When the impurities reach those sites, possibly by vacancy-aided diffusion, they no longer

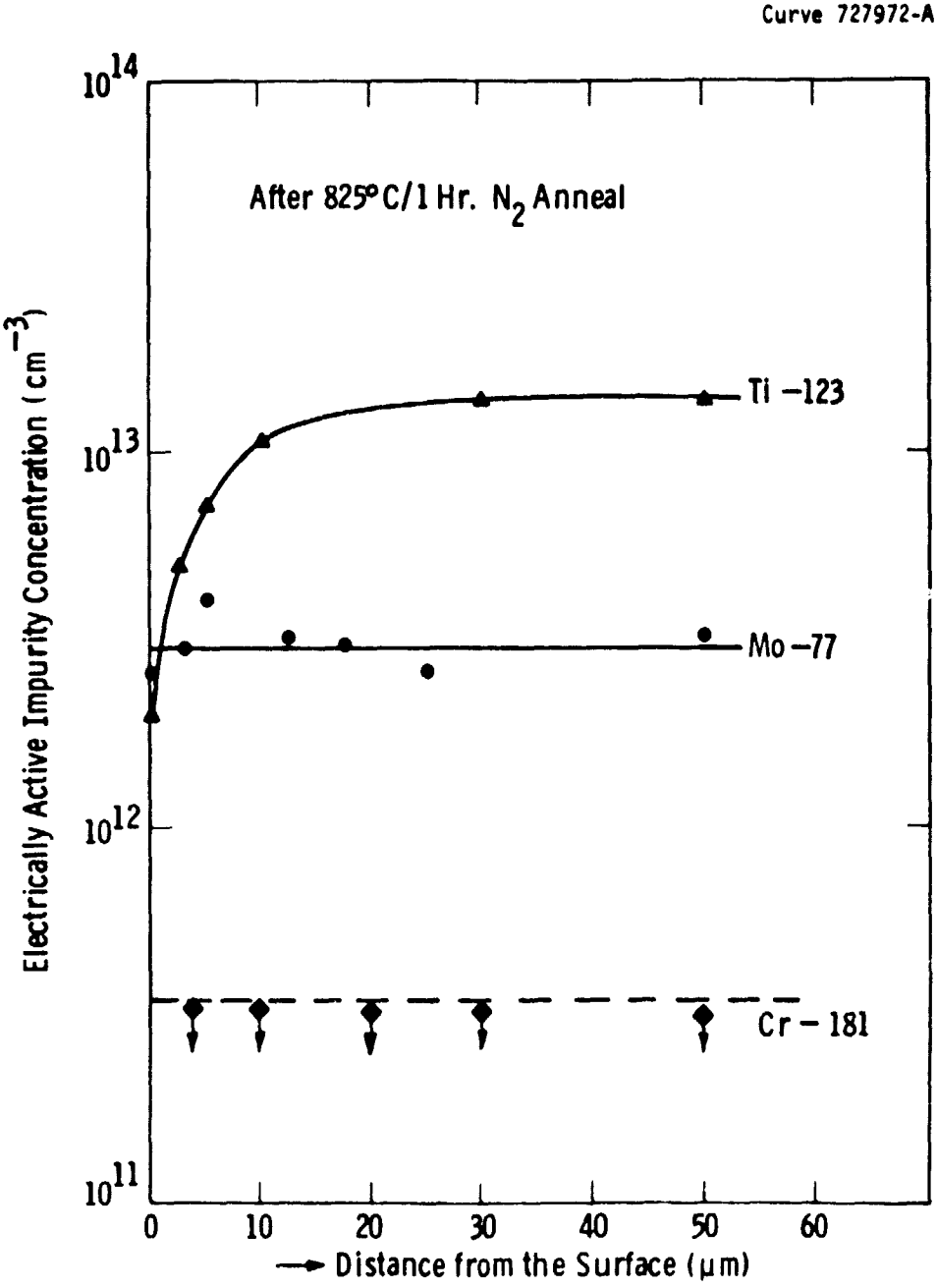

Figure 14 Change in electrically active impurity concentration after an 825°C/1-hour N_2 anneal.

Curve 727973-A

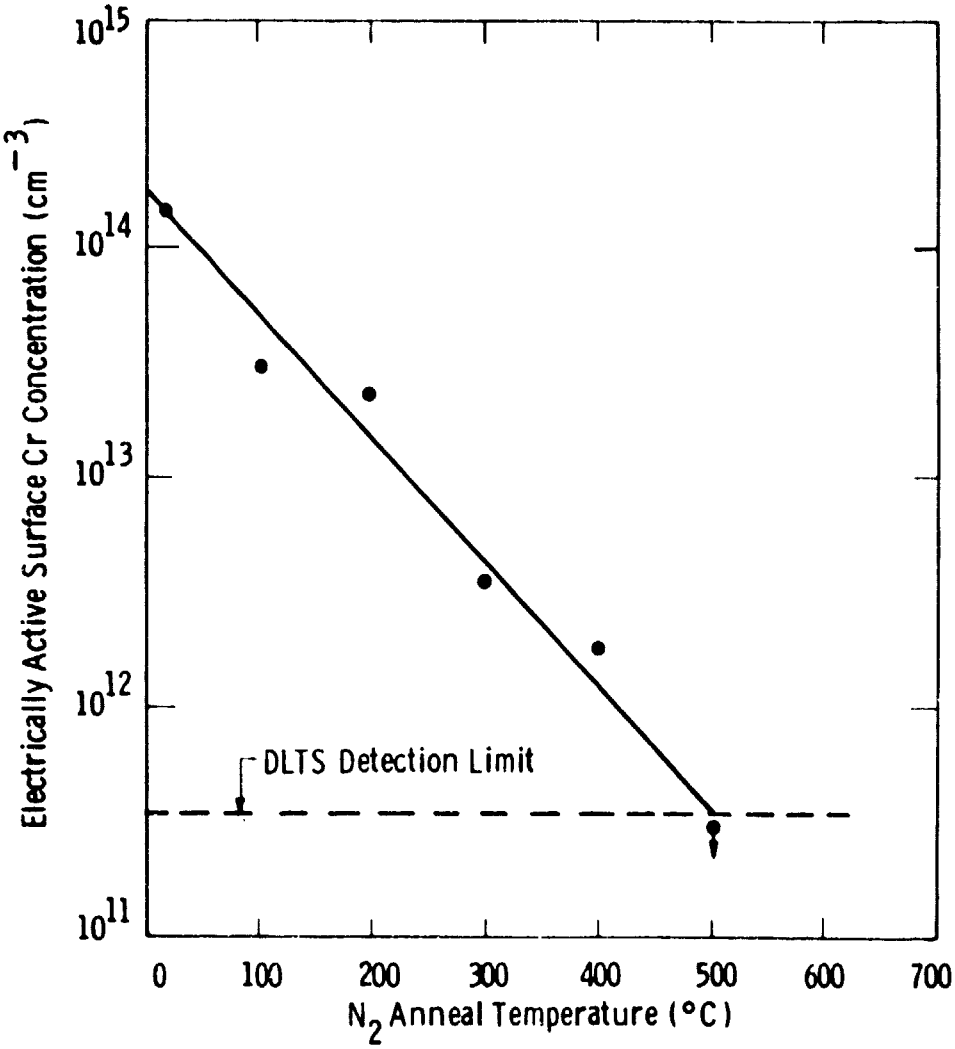

Figure 15 Variation of electrically active Cr concentration following a one-hour treatment in N_2.

TABLE 11

THE EFFECT OF N_2 HEAT TREATMENT ON THE ELECTRICALLY ACTIVE Cr CONCENTRATION AT THE SURFACE OF WAFERS CONTAINING 1×10^{15} cm^{-3} METALLURGICAL Cr.

Annealing Condition	Active Cr Concentration at the Surface (cm^{-3})
None	1.5×10^{14}
100°C/1 hr	3.0×10^{13}
200°C/1 hr	2.4×10^{13}
300°C/1 hr	3.5×10^{12}
400°C/1 hr	1.9×10^{12}
500°C/1 hr	undetectable
600°C/1 hr	undetectable
825°C/1 hr	undetectable

TABLE 12

DLTS RESULTS ON IMPURITY-DOPED INGOTS

Ingot ID	Best Estimate of Metallurgical Impurity Concentration (N_M)	Active Impurity Concentration (cm^{-3})		
		In the Wafer N_{TW}	In the Cell (near junction) N_{TC}	$\frac{N_{TW}}{N_M}$
V-200-Poly	4×10^{14}	1.3×10^{14}	no data	0.32
Ti-202-Poly	2×10^{13}	1.12×10^{13}	1.15×10^{12}	0.56
V-203-Poly	4×10^{13}	1.7×10^{13}	undetectable	0.34
206-V	2.6×10^{13}	6.43×10^{12}	undetectable	0.25
207-Mo	2.0×10^{13}	2.2×10^{12}	9×10^{11}	1.1
208-Cr	1.9×10^{14}	3.91×10^{13}	undetectable	0.21
209-Ti	2.0×10^{13}	8.12×10^{12}	1.15×10^{12}	0.40
210-Ti	1.0×10^{14}	2.91×10^{13}	3.6×10^{12}	0.30
211-Cu	1.8×10^{15}	undetectable	undetectable	-
212-Cu	1×10^{16}	undetectable	undetectable	-
214-V-Poly	2×10^{14}	6×10^{13}	no data	0.30
215-Mo-Poly	2.5×10^{12}	4.5×10^{12}	no data	1.8
216-Cr-Poly	8×10^{14}	7.5×10^{12}	no data	.009
217-Ta	1.5×10^{11}	undetectable	undetectable	-
218-Ta	6.5×10^{10}	undetectable	undetectable	-
222-Ag	4.5×10^{15}	undetectable	undetectable	-
223-Ni	1.0×10^{15}	undetectable	undetectable	-
225-Mn	1.0×10^{15}	undetectable	undetectable	-
227-Cr-Poly	4.0×10^{14}	1.2×10^{13} average	undetectable	0.03
228-Gd	-	undetectable	undetectable	-
229-Au	6.0×10^{14}	8×10^{13}	undetectable	0.13
230-Al	1.2×10^{17}	2×10^{12}	6.3×10^{13}	0.000016
231-Mn-Poly		undetectable	undetectable	

act like electrically active recombination centers. Our model for $POCl_3$ gettering[3] assumed that Ti forms a complex with phosphorus and acquires a different energy site which is no longer a part of the electrically active population. This results in a concentration gradient directed toward the phosphorous-rich region and leads to a depletion of impurity in the p-region.

In order to determine the similarities and differences between the response of Ti impurity to the $POCl_3$ and N_2 treatment, several experiments are being performed at higher temperature on the same material, ingot Ti-123. We also further explored the strong thermal response of Cr activity by heat treating the Cr-doped wafers in a N_2 ambient in the temperature range of 100-600°C. The treatment time was one hour in all cases. After heat treatment, 30-mil diameter Ti-Au Schottky barrier diodes were fabricated to detect the active Cr concentration at the wafer surface via DLTS. The results of these experiments are shown in Table 11 and Figure 15. Even after the 100°C treatment, we detect about a factor of 5 loss in the electrical activity of Cr at the surface. After a 400°C anneal, a loss of two orders of magnitude in electrical activity was observed.

As found previously in the $POCl_3$ gettering experiments, nearly a complete loss of Cr electrical activity occurs after a 500-600°C heat treatment. The data therefore suggest that the loss of Cr electrical activity during $POCl_3$ gettering is largely an effect of thermal treatment. Some effect due to phosphorous cannot be ruled out, however. To gain a clearer insight into the mechanism of this loss of activity, we are conducting an experiment to determine the Cr concentration profile, if any, formed between the surface and the bulk during heat treatment.

3.4 Solar Cell and Material Evaluation by DLTS

We continue to monitor the electrically active impurity concentrations of representative wafers (as-grown) and solar cells to correlate device and materials effects due to impurities. Table 12 is an up-to-date summary of information collected by deep-level transient spectroscopy for single and polycrystalline ingots. We have found no levels for Cu, Ta, Ag, Ni, Mn.

3.5 Impurity Effects in High-Efficiency Solar Cells

In previous reports[3,V2] we have presented mathematical analyses of both the standard process devices and of several high-efficiency devices (see, e.g., Tables 13 and 14). A finite element cell model was used to establish that the simple impurity model equations could provide reasonably accurate predictions of impurity/performance effects in high-efficiency cells. Data from two of these model calculations are shown in Figures 16 and 17. The agreement is quite good particularly for low to moderate impurity concentrations.

Other calculations have shown that high-efficiency (HE) devices, in general, require long diffusion lengths and therefore may be expected to be more sensitive to impurity degradation than are standard efficiency (SE) cells. That is, the degradation threshold (N_{0X}) for a given impurity will be smaller for HE cells than for SE cells. We expect this increased sensitivity to be observed for wide-base cells and for medium-base cells using back surface fields and passivated surfaces. This situation, however, can be reversed to a degree by making devices with narrow base widths, although, by doing so may lower the short-circuit current and efficiency because of reduced spectral absorption. The performance tradeoff is small for basewidths down to approximately 100μm and such devices are included in our experiments for this reason (Table 14).

Experimental data to support these analytic results have been slow in coming because the HE devices are much more demanding of the process technology and accutely sensitive to effects which go unnoticed in SE cells. Four experimental runs of wide-base and medium-base devices were completed which failed to achieve their design performance and therefor yielded only a small amount of useful data.

Recently, however, narrow-base HE cells have been made with efficiencies in the 14.5% to 15.5% range. Data from two of these experiments for narrow-base cells, types 1 and 2 (see Table 14) are given in Table 15 and 16. These devices have a base width of 100μm and are expected to have reduced sensitivity to the impurity, i.e., a larger value

TABLE 13

PROPERTIES OF STANDARD PROCESS CELLS

STANDARD EFFICIENCY CELLS (SE)

P-Base: 3-5Ωcm (N_A 3.5 x $10^{15}/cm^3$)

Base Width: ∿ 275μm

Cell Area: $1.032cm^2$

Front Junction: Phosphorus Diffused, X_j ≈ .3μm

Contact Grid: ∿ 5.3% coverage, Ti-Pd-Ag.

No AR coating

No BSF

Ohmic Back: Ti-Pd-Ag

TYPICAL PERFORMANCE (∿AM1, $91.6mW/cm^2$) (No AR coating)

J_{SC} = 21.8mA, V_{OC} = .556Volts, FF = .78, EFF = 9.5%

Effective Base diffusion length ≈ 175μm

Effective Base Lifetime ≈ 9μs

TABLE 14

HIGH-EFFICIENCY CELL TYPES UNDER INVESTIGATION

Wide Base	1	$W_B \geq 750\mu m$	No AR	Ohmic Back
	2		With AR*	
Medium Base	1	$W_B \triangleq 275\mu m$	With AR*	Ohmic Back
	2			Gridded Back - No passivation of back surface
	3			Gridded Back - with passivation
Narrow Base	1	$W_B \leq 150\mu m$	No AR	Ohmic Back
	2			Gridded Back - No passivation of back surface
	3			" - with passivation
	4		With AR*	" "

Base material is P-type 3-5 ohm-cm ($N_A \triangleq 3.5 \times 10^{15}/cm^3$)

Front junction is phosphorus diffused with X_j = .25 to .35μm

*AR coating process includes passivation of exposed front surface.

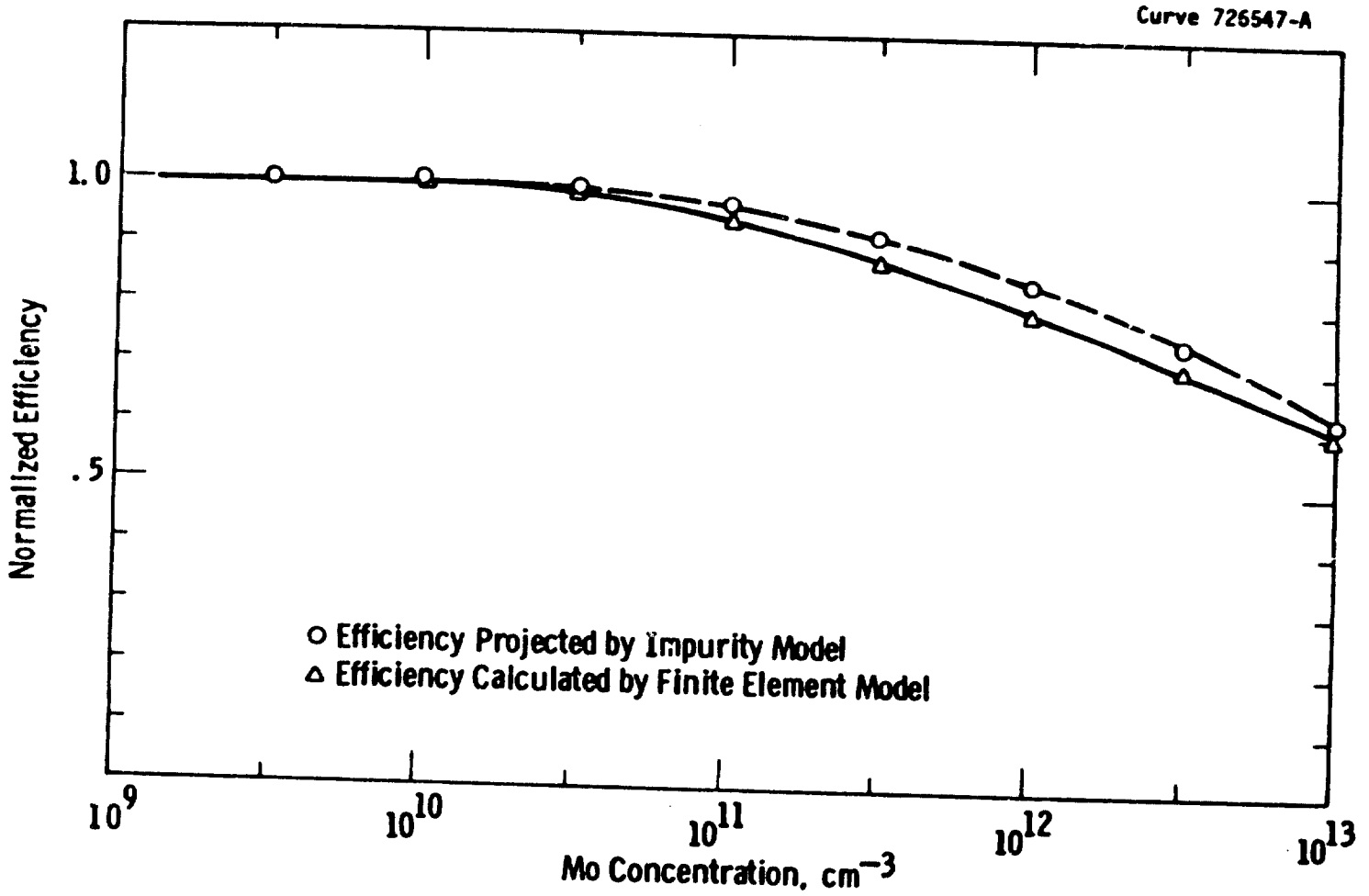

Figure 16 Calculated Cell Efficiency as a Function of Molybdenum Concentration for a Standard (SE) Design Cell (η = 14%, W_B = 275μm.)

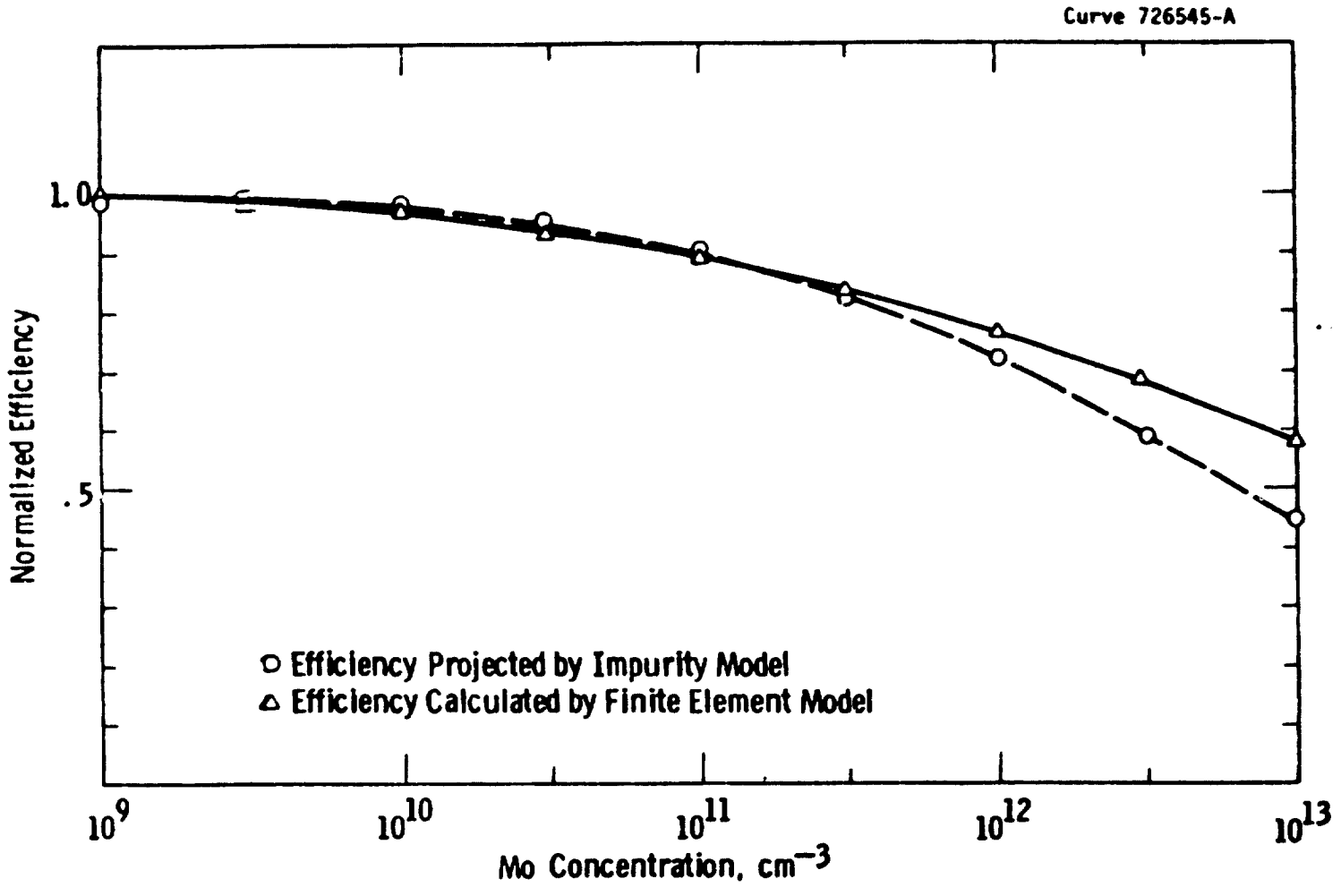

Figure 17 Calculated Efficiency as a Function of Molybdenum Concentration for a Narrow Base, Back Surface Field HE Cell (η = 15.35%, W_B = 150μm).

TABLE 15

100μm CELLS WITH BSF AND OHMIC BACKS, AVERAGED DATA

	J_{SC}	V_{OC}	FF	E_{FF}	L_n	I_n	N_x	N_{OX}	
W198 Base line	21.00	.546	.755	9.46	140	1	0	3.91×10^{12}	(1)
W206V006	19.10	.528	.750	8.05	64	.909	2.6×10^{13}	5.4×10^{12}	(2)
								4.50×10^{12}	(3)
W219V008	20.48	.556	.750	9.03	101	.975	9×10^{12}	4.68×10^{12}	(2)
								3.51×10^{12}	(3)

Notes (1) predicted from base line data using Equation (4)

(2) calculated from diffusion length data using Equation (8)

(3) calculated from short-circuit current data using Equation (10)

TABLE 16

100μm CELLS WITH BSF AND GRIDDED BACK (See text), AVERAGED DATA.

	J_{SC}	V_{OC}	FF	E_{FF}	L_n	I_n	N_x	N_{OX}	
W198 Base line	21.80	.572	.772	10.51	-	1	0	-	
W206V006	19.4	.540	.747	8.54	-	.88	2.6×10^{13}	3.9×10^{12}	(2)
W219V008	20.02	.560	.773	9.42	-	.918	9×10^{12}	2×10^{12}	(2)

Note (2) Calculated from I_n and N_x using Equation (6).

of the degradation threshold than is observed in SE cells. The impurity in these samples is vanadium, which has a threshold in SE cells: N_{OX} = $2.5 \times 10^{12}/cm^3$. Referring to the impurity model derivation in Reference 3, V2 p30ff., we can express the threshold as:

$$N_{OX} = \frac{D_n}{L_{no}^2 V_{th} \sigma_x A_x} \tag{3}$$

where D_n is the minority-carrier diffusivity in the base.

L_{no} is the effective minority diffusion length in impurity free cells.

V_{th} is the thermal velocity.

σ_x is recombination cross-section for impurity x.

A_x is the fraction part of the impurity atoms which are electrically active.

Using Equation (3) we obtain:

$$N_{OX}(HE) = N_{OX}(SE) \left[\frac{L_{no}(SE)}{L_{no}(HE)}\right]^2 \tag{4}$$

The other parameters of Equation (3) vanish because the base material is the same for both devices, and we are considering the same impurity in both cases.

For ohmic back devices $L_{no}(SE) = 175\mu m$, $L_{no}(HE) = 140\ \mu m$, and $N_{OX}(V) \doteq 2.5 \times 10^{12}/cm^3$, so we find:

$$N_{OX(V)}(HE) = 3.91 \times 10^{12}\ cm^{-3}$$

A second method of calculating the threshold utilizes the effective diffusion lengths in the impurity containing HE cells. We can relate the diffusion length to the lifetime:

$$L_n^2 = D_n \tau_n \tag{5}$$

and using Shockly-Reed recombination theory

$$\tau_n = \frac{1}{\sigma_x N_{th} N_T} \tag{6}$$

where N_T = the density of recombination centers.

We have shown previously for a given impurity x that $N_T = A_x N_x$ so that:

$$L_n^2 = \frac{D_n}{\sigma_x V_{th} N_x A_x} \tag{7}$$

Now substituting Equation (5) in Equation (3) we obtain:

$$N_{OX} = \left(\frac{L_n}{L_{no}}\right)^2 N_x \tag{8}$$

Using the diffusion length and impurity concentration data in Table 15 we get for Ingot W206V006:

$$N_{OX} = 5.40 \times 10^{12}/cm^3$$

and for W219V008:

$$N_{OX} = 4.68 \times 10^{12}/cm^3$$

The degradation threshold may be calculated a third way from the measured short-circuit current of cells containing a known impurity concentration. The relationship between these quantities is given by the impurity model equation[3].

$$\left(\frac{I_{no}}{I_n} - 1\right)^2 = C_1\left(1 + \frac{N_x}{N_{ox}}\right) \tag{9}$$

where $I_{n\infty}$ = 1.11 is a model constant, being the normalized short-circuit current which would be observed if the diffusion length were infinite,

I_n = is the normalized current for a cell with impurity concentration N_x, and

C_1 = is a model constant = 0.0121.

All measured currents are normalized by the measured short-circuit current of base line cells.

Solving Equation (5) for N_{OX} gives:

$$N_{OX} = \frac{N_x}{\frac{1}{C_1}\left(\frac{I_{n\infty}}{I_n} - 1\right)^2 + 1} \qquad (10)$$

Using Equation (6) and the data in Table 15, for cells from Ingot W206V006 we obtain:

$$N_{OX}(V) = 4.5 \times 10^{12}$$

and from Ingot W219V008:

$$N_{OX}(V) = 3.5 \times 10^{12}$$

The predicted and experimental values of the threshold are in fairly good agreement and confirm, as expected, that these thin base cells are less sensitive to impurity contamination.

Following the experiment of Table 15, the metal backs of these cells were photo-masked and etched so as to leave a back contact grid--that is, leaving only about 5% of the cell back covered with metal with the remainder of the back surface being bare silicon. This has the effect of significantly reducing the effective surface recombination velocity of the back. The metal-covered surface has an $S_o \doteq 10^6$ cm/s,

while the bare silicon has an $S_o \approx 5 \times 10^3$ cm/s. Based on model calculations, a reduction in S_o should improve the effectiveness of the BSF and result in increased efficiency. This is borne out by the experimental data shown in Table 16. The baseline cell efficiencies increased approximately one percentage point while the efficiencies of the vanadium-containing cells increased somewhat less.

Diffusion length data are not available for these cells, but values of N_{OX} are calculated from the short-circuit current data using Equation (6). The results are shown in Table 16, with the values straddling the value obtained for SE cells. We know from the increased short circuit that these devices have longer effective diffusion lengths than those of Table 15; consequently, it should be expected that a smaller threshold concentration be observed. It should be noted that attrition due to breakage of the very fragile 100μm-thin cells left us a statistically small number of samples and thus larger uncertainty than in the previous experiment. Diffusion length data for these samples will be available soon and will help clarify the results.

The data from these experiments are in fairly good agreement with the analytic models and further confirm the usefulness of the impurity model equations to estimate the impact of impurities on HE cell performance. Several experiments are in progress using several of the HE designs to complete the verification of the analytical predictions.

4. CONCLUSIONS

Structural breakdown of silicon ingots caused by impurities in the melts from which the ingots grew takes place at a lower impurity concentration (at least for Cr, Mo, and Fe) in ingots which contain mm-sized grains than it does when single crystals are growing. This is consistent with the idea that grain boundaries act as sites where structural instabilities can initiate.

Liquid diffusion constants calculated from structural breakdown data fall in the range 1 to 4 x 10^{-4} cm^2/sec for most of the impurities we have studied. Although the breakdown model is too simple to expect precise values of D_ℓ, the calculated values are close to those measured for other impurities in silicon.

Preliminary data show that for Ag and Cr, deep levels develop with time as the metal-doped solar cells are aged at elevated temperatures. This may suggest one of the mechanisms that operates to reduce cell efficiency is minority-carrier lifetime depreciation by deep-level formation.

Ion implant damage is a relatively poor technique to getter impurities and raise cell efficiency compared to the more commonly employed HCℓ or $POCℓ_3$ treatments. The argon treatment alone raises the efficiency of Ti-doped cells slightly and the efficiency of Cu-doped cells not at all. In combination with HCℓ or $POCℓ_3$ treatment, implant damage raises cell efficiency, but again the chemical treatments by themselves are more effective.

Low-temperature (100-600°C) heat treatments can partly or completely eliminate the electrically active concentration of Cr in silicon. The mechanism for this effect is not yet known but probably involves Cr precipitation to form a new phase or possibly shift of Cr atoms to a different lattice site.

Solar cells made on 100 μm-thick V-doped wafers exhibit thresholds for impurity-induced efficiency degradation which are consistent with model predictions. Some increase in threshold is noted, since impurity sensitivity is not as severe as that which occurs in wide-base, high-efficiency cells with a similar impurity concentration.

5. PROGRAM STATUS

The current milestone chart for the Phase IV program is illustrated in Figure 18.

5.1 Present Status

During this quarter we:

- Evaluated the relative effects of liquid-impurity concentration on structural breakdown in poly and single crystal ingots.
- Calculated liquid-diffusion constants near the melting point of silicon for many of the metal impurities studied during this program.
- Completed low-temperature solar cell bias/aging tests to 245°C.
- Evaluated the mechanism of performance reduction for Ag and Cr-doped solar cells aged at high temperature.
- Evaluated the effectiveness of Ar ion implant damage alone and coupled with HCℓ and $POCℓ_3$ as a gettering technique for harmful impurities.
- Measured the electrical activity of Cr, Ti and Mo following heat treatment in N_2.
- Assessed the behavior of V in high-efficiency thin cells.

5.2 Future Activity

During the next quarter we will complete the remaining program activities.

Figure 18

PHASE IV PROGRAM PLAN (SCHEDULE)

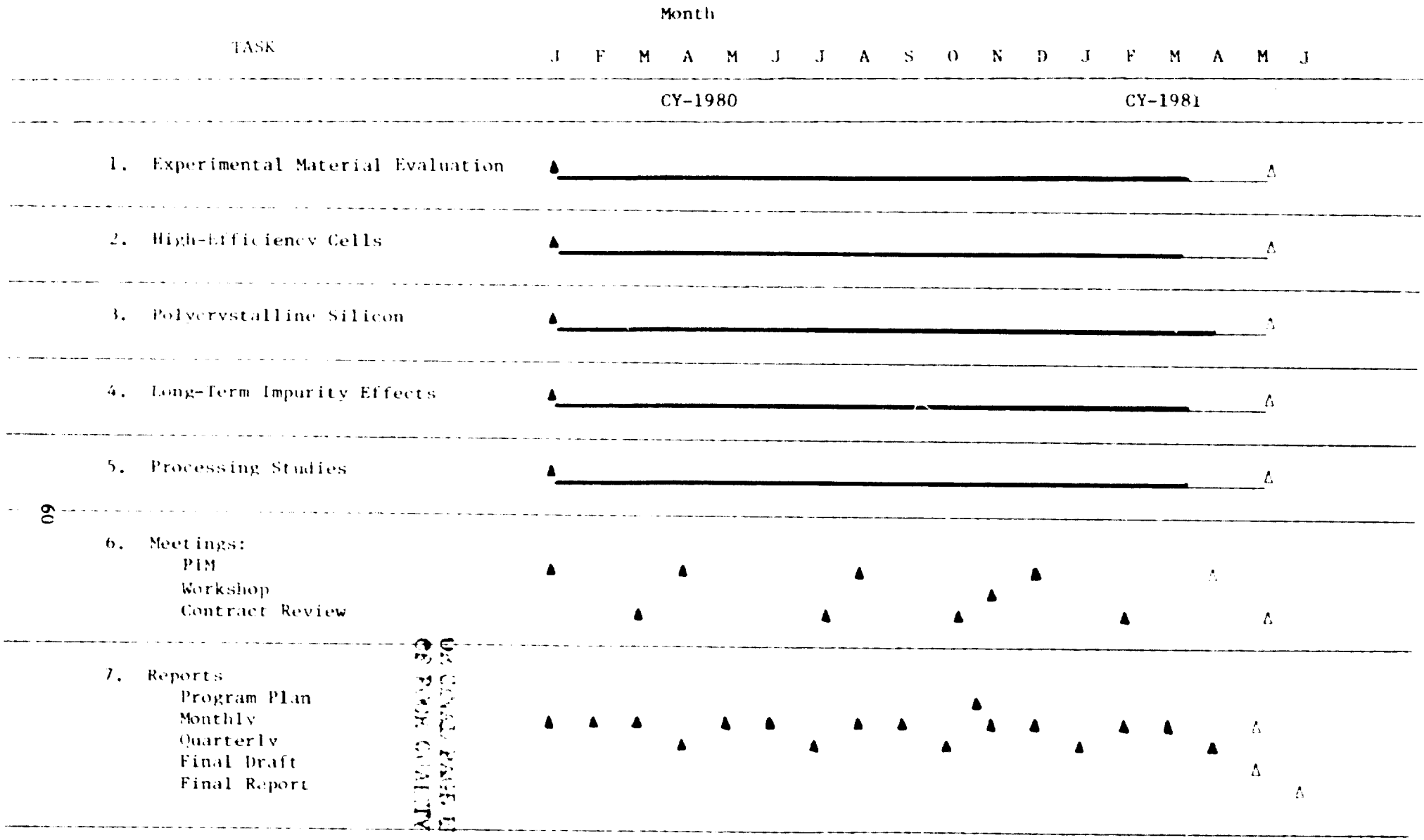

6. REFERENCES

1. R. H. Hopkins, et al., 11th Quarterly Report and Summary, Silicon Materials Task (Part 2) DOE/JPL 954331-78/3 (July 1978).

2. R. H. Hopkins, et al., 5th Quarterly Report and Summary, Silicon Materials Task (Part 2) DOE/JPL 954331-77/1 (January 1977).

3. R. H. Hopkins, et al., 17th Quarterly Report and Summary-Volume 1 and 2, Silicon Materials Task (Part 2) DOE/JPL 954331-80/9 (January 1980).

4. K. Graff. et al., Solid St. Elect. 16, 887 (1973).

5. Silicon Semiconductor Technology. W. R. Runyun, McGraw-Hill, NY (1965) pp. 58, 59.

6. R. H. Hopkins, et al. 17th Quarterly Report and Summary, Volume 2 (Analysis of Impurity Behavior). Silicon Materials Task. DOE/JPL-954331-80/9. (January 1980).

7. H. Kodera, Japanese J. Appl. Physics, 2, 212 (1963).

8. T. G. Digges and R. Shima, J. Crystal Growth, 50, 865 (1980).

9. A. G. Milnes, Deep Impurities in Semiconductors, New York Wiley (1973).

10. R. H. Hopkins, et al., 21st Quarterly Report, Silicon Material Task (Part 2) DOE/JPL-954331-81/13 (April 1981).

7. ACKNOWLEDGEMENTS

We would like to thank the following individuals whose contributions have been important to the success of this program: D. N. Schmidt (cell processing and testing), B. F. Westwood and J. McNally (process experiments and photolithography), A. M. Stewart (material characterization), H. F. Abt (metallization), S. Karako (DLTS measurements), T. Zigarovich (mask preparation), R. R. Adams and J. M. Bronner (processing), and D. Labor (manuscript preparation).